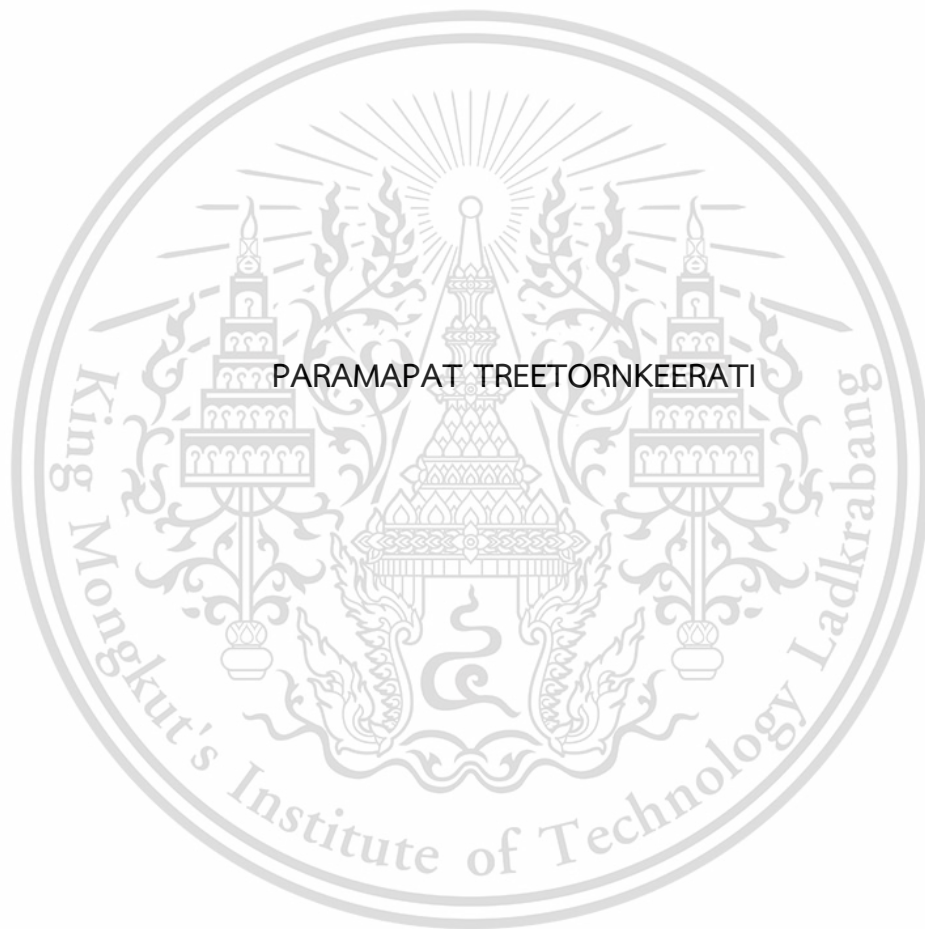


SYNTHESIS OF ALUMINUM TITANATE COMPOSITE
AND ITS CORROSION BEHAVIOR IN MOLTEN ALUMINUM



A THESIS SUBMITTED IN PARTIAL FULFILLMENT OF THE REQUIREMENT FOR THE
DEGREE OF MASTER OF SCIENCE IN APPLIED PHYSICS
DEPARTMENT OF PHYSICS SCHOOL OF SCIENCE
KING MONGKUT'S INSTITUTE OF TECHNOLOGY LADKRABANG
2023

KMITL-2023-SC-M-030-078

This material is reserved for educational use only, not allowed for commercial use.

Forbidden to modify the content, and cite the document when use.



COPYRIGHT 2023

SCHOOL OF SCIENCE

KING MONGKUT'S INSTITUTE OF TECHNOLOGY LADKRABANG

This material is reserved for educational use only, not allowed for commercial use.

Forbidden to modify the content, and cite the document when use.

Thesis Title	Synthesis of Aluminum Titanate Composite and Its Corrosion Behavior in Molten Aluminum
Student Name	Paramapat Treetornkeerati
Student ID	63605034
Degree	Master of Science (Applied Physics)
Department	Physics
Year	2566
Thesis Advisor	Assistance Professor Dr. Mettaya Kittivan
Thesis Co-advisor (if any)	Dr. Supawan Vichaphund

Abstract

This research aims to investigate the effects of hexagonal boron nitride (h-BN) and aluminum nitride (AlN) additives on the properties of aluminum titanate composite (Al_2TiO_5 : AT). The results indicated that the content of both additives has an impact on phase formation, bulk density, porosity, mechanical properties, microstructure, and corrosion resistance in molten aluminum. The X-ray diffraction (XRD) analysis reveals the formation of aluminum borate ($\text{Al}_{18}\text{B}_4\text{O}_{33}$) in the AT composites with h-BN (ATBN), while the presence of titanium nitride (TiN) alongside AT and Al_2O_3 is caused by the incorporation of AlN in AT (ATN). For h-BN addition, the ATBN20 composition exhibited the highest bulk density at 3.12 g/cm^3 and improved mechanical properties, achieving a flexural strength of 123.62 MPa and a Vickers hardness of 11.15 GPa. Furthermore, the addition of AlN contributes to an increase in bulk density, with A50TN exhibiting the highest value at 3.81 g/cm^3 , which is correlated with the highest flexural strength of 249.12 MPa and Vickers hardness and 12.87 GPa. Microstructural analysis confirms the role of both additives in reducing pores and contributing to enhanced properties. In the corrosion analysis in molten Al, the A50TN sample exhibited the most suitable corrosion resistance with the thinnest layers of $0 \text{ }\mu\text{m}$, $120.87 \text{ }\mu\text{m}$, and $247.76 \text{ }\mu\text{m}$ over the 4, 24, and 48 h, respectively. The study establishes h-BN and AlN as effective additives for optimizing the properties of AT composites, offering promising prospects for diverse industrial applications.

Keywords: Aluminum Titanate, Hexagonal boron nitride, Aluminum nitride, molten Aluminum, Mechanical properties

This material is reserved for educational use only, not allowed for commercial use.

Forbidden to modify the content, and cite the document when use.

Acknowledgements

The generosity and support of many people in a variety of fields made this thesis possible. This provides us with opportunities and inspiration, which ultimately results in the success of this thesis. Thus, I would like to sincerely thank each and every one of you in the manner described below:

First of all, I would like to express my deepest gratitude to my advisor, Asst. Prof. Dr. Mettaya Kitiwan and co-thesis advisor Dr. Supawan Vichaphund, as well as Asst. Prof. Dr. Phacharaphon Tunthawiroon for their advice, encouragement, and support throughout the research process. Their insights played a key role in shaping this dissertation.

I am grateful to the team at MTEC and at the equipment centers, who often give help and recommendations for entering the lab each time. This thesis cannot be completed. Without everyone's help, thank you very much.

A special thanks to my colleagues and friends. It's my thanks for offering help and encouragement during challenging times. It is also a part that makes this trip more enjoyable.

Finally, I would like to express my deep gratitude to my family for their unwavering love, understanding, and encouragement. Their support has been an important part of my educational journey.

This thesis would not have been possible without the combined efforts of these individuals and organizations. Thank you all for being an important part of this academic endeavor.

Miss Paramapat Treetornkeerati

This material is reserved for educational use only, not allowed for commercial use.

Forbidden to modify the content, and cite the document when use.

Table of contents

	Page
Abstract in English	I
Acknowledgements	II
Table of contents	III
List of tables	V
List of figures	VI
Chapter 1 Introduction	1
1.1 Research motivation	1
1.2 Objectives of the study	2
1.3 Scopes of the study	2
1.4 Benefits of the study	2
Chapter 2 Theory and literature reviews	3
2.1 Properties of starting materials	3
2.1.1 Alumina (Al_2O_3)	3
2.1.2 Titanium dioxide (TiO_2)	4
2.1.3 Hexagonal boron nitride (h-BN)	6
2.1.4 Aluminum nitride (AlN)	7
2.2 Aluminum titanate (Al_2TiO_5 : AT)	8
2.2.1 Structural, properties and applications	8
2.2.2 Limitation of monolithic aluminum titanate	10
2.3 Effect of oxide addition on thermal stability and mechanical properties of aluminum titanate	11
2.4 Improving of mechanical properties by formation of aluminum titanate composites	13
2.5 Corrosion behavior of AT composites in molten Al	14
Chapter 3 Research methodology	15
3.1 Chemicals and equipment	15
3.1.1 Chemicals	15
3.1.2 Tools and equipment	16

	Page
3.2 Experimental procedures	17
3.2.1 Procedure for preparation of AT/h-BN composite samples	17
3.2.2 Procedure for preparation of AT/AlN composite samples	20
3.3 Sample characterizations	20
3.3.1 Phase transition analysis	21
3.3.2 Densification analysis	22
3.3.3 Microstructural and chemical analysis	24
3.3.4 Flexural strength analysis	24
3.3.5 Hardness analysis	26
3.3.6 Coefficient of thermal expansion (CTE) analysis	27
3.3.7 Corrosion behavior in molten Al analysis	28
Chapter 4 Results and discussion	30
4.1 AT composite with h-BN addition	30
4.1.1 Phase transition analysis (XRD)	30
4.1.2 Physical properties (Bulk density and porosity)	32
4.1.3 Microstructure and chemical analysis (SEM, EBSD)	33
4.1.4 Mechanical properties (Flexural strength and Vickers hardness)	34
4.1.5 Thermal properties (CTE)	37
4.2 AT composite with AlN addition	39
4.2.1 Phase transition analysis (XRD)	39
4.2.2 Physical properties (Bulk density and porosity)	40
4.2.3 Microstructure and chemical analysis (SEM, EBSD)	42
4.2.4 Mechanical properties (Flexural strength and Vickers hardness)	44
4.2.5 Corrosion behavior in Molten Al	45
Chapter 5 Conclusion and suggestion	54
References	55
Author biography	60

List of tables

Table	Page
2.1 Typical properties of aluminum oxide (Al_2O_3)	4
2.2 Properties of titanium dioxide (TiO_2) in different crystal phases	5
2.3 Properties of aluminum titanate (Al_2TiO_5 , AT)	9
3.1 Raw materials and chemicals used in experiments.	15
3.2 Tools and equipment used in experiment	16
3.3 Compositions of the starting powders used for AT/h-BN composite	18
3.4 Compositions of the starting powders used for AT/AlN composite	20
3.5 Measurement parameters for X-ray diffraction phase analysis	21
3.6 Chemical composition (in wt.%) of ADC 12 alloy	28
4.1 Bulk density and porosity of AT/h-BN samples	33
4.2 Flexural strength and Vickers hardness of AT/h-BN samples	36
4.3 Bulk density and porosity of AT/AlN samples	41
4.4 Flexural strength and Vickers hardness of AT/AlN samples	44

List of figures

Figure	Page
2.1 Crystal structure of aluminum oxide (Al_2O_3)	3
2.2 Crystal structures of titanium dioxide (TiO_2): (a) rutile; (b) brookite, and (c) anatase	5
2.3 Crystal structure of (a) graphite and (b) hexagonal boron nitride (h-BN),	6
2.4 Crystal structure of aluminum nitride (AlN)	7
2.5 Crystal structure of aluminum titanate (Al_2TiO_5)	8
2.6 Phase diagram of Al_2O_3 - TiO_2 system	9
2.7 Applications of aluminum titanate, (a) riser tubes, (b) breakrings, (c) nozzles/bushes, (d) stopper/plates, (e) diesel particulate filter (DPF), and (f) water filter	10
3.1 Schematic of the preparation of AT/h-BN composite samples	17
3.2 (a) Hydraulic pressing machine (IPH1240, ENERPAC), and (b) set of molds used in the forming process.	19
3.3 High-temperature furnace machine	19
3.4 The heating profile for sintering AT composites	19
3.5 Flow chart of characterizations and properties measurements	21
3.6 X-ray diffractometer (XRD)	22
3.7 Weighing Scale for measuring Archimedes	23
3.8 The experimental schematic of Archimedes' method	23
3.9 Scanning electron microscopy (SEM)	24
3.10 Universal testing machine	25
3.11 Schematic of the 3-point flexural strength test	26
3.12 Vickers Hardness Testing Machine	27
3.13 (a) Schematic operation principles of the Vickers hardness machine and (b) the measurement of impression diagonals	27
3.14 Dilatometer used to measure CTE of all composite samples	28
3.15 The experimental setup for an immersion test in molten Al	29
3.16 Metallurgical mounting press machine	29

Figure	Page
4.1 The XRD patterns of sintered AT and ATBN composites	31
4.2 The bulk density (black graph) and porosity (blue graph) of samples with different h-BN content.	34
4.3 BSE-SEM images of polished surface of (a) AT, (b) ATBN5, (c) ATBN10, (d) ATBN15, (e) ATBN20, and (f) ATBN30. The inset image in each figure represents a high magnification of a rectangular area.	35
4.4 The effect of h-BN content on the flexural strength of Al_2TiO_5 composites	37
4.5 The effect of h-BN content on the Vickers hardness of Al_2TiO_5 composites	37
4.6 The effect of h-BN content on the CTE of Al_2TiO_5 composites	38
4.7 X-ray diffraction patterns of samples with different Al_2O_3 content	40
4.8 The bulk density (black line) and porosity (blue line) of samples with different Al_2O_3 content	42
4.9 EBSD-SEM micrograph of A30TN sample	43
4.10 BSE-SEM micrograph of samples with different Al_2O_3 content	43
4.11 Flexural strength (black graph) and Vickers hardness (blue graph) of samples	45
4.12 SEM image from the cross-section of the A30TN composite sample after immersion in molten Al at 720 °C for 4 h	46
4.13 SEM image from the cross-section of the A30TN composite sample after immersion in molten Al at 720 °C for 24 h	47
4.14 SEM image from the cross-section of the A30TN composite sample after immersion in molten Al at 720 °C for 48 h	47
4.15 SEM image from the cross-section of the A40TN composite sample after immersion in molten Al at 720 °C for 4 h	48
4.16 SEM image from the cross-section of the A40TN composite sample after immersion in molten Al at 720 °C for 24 h	49
4.17 SEM image from the cross-section of the A40TN composite sample after immersion in molten Al at 720 °C for 48 h	49
4.18 SEM image from the cross-section of the A50TN composite sample after immersion in molten Al at 720 °C for 4 h	50
4.19 SEM image from the cross-section of the A50TN composite sample after immersion in molten Al at 720 °C for 24 h	51

Figure	Page
4.20 SEM image from the cross-section of the A50TN composite sample after immersion in molten Al at 720 °C for 48 h	51
4.21 Comparison of the corrosion behavior of molten Al in all composites sample at 720 °C for 4, 24 and 48 h.	52
4.22 Plot of thickness of corroded layer in each range of all composite sample at 720°C.	53



Chapter 1

Introduction

1.1 Research motivation

Ceramics are widely employed in various fields such as industrial, engineering, medical, and aerospace due to their excellent properties like high hardness, low density, high corrosion resistance, and high wear resistance. However, they are severely limited by brittleness [1-2]. In general, the second phase such as particles or fibers are added into the ceramic matrix to produce fracture deflection and improve toughness to overcome the brittleness of traditional ceramics [3].

Aluminum titanate (Al_2TiO_5 : AT) is a refractory ceramic that has recently received a lot of attention. AT has great thermal properties, such as a high melting point, a low thermal expansion coefficient, and a high resistance to thermal shock and high-temperature corrosion resistance. Therefore, it is a prospective material to use at elevated temperatures, especially in sudden temperature changes condition. At present, AT is used in many fields of industry, for example, as a filter material for exhaust soot in Diesel engines (Diesel particulate filter: DPF) and the crucible in metal smelting industry [4-8].

However, AT has two apparent drawbacks which limit its application. The thermal instability of AT tends to decompose to Al_2O_3 and TiO_2 at the temperature range of 750–1300°C, and the low mechanical strength due to microcracks generated from anisotropy of thermal expansion coefficients of AT [9-10]. Many studies have been done on the doping of various oxide additives such as MgO , Fe_2O_3 , SiO_2 , and ZrO_2 [11-13] as well as compounds such as spodumene (LiAlSiO_4), mullite ($3\text{Al}_2\text{O}_3 \cdot 2\text{SiO}_2$), cordierite ($\text{Mg}_2\text{Al}_4\text{Si}_5\text{O}_{18}$), and feldspar [14-17], into AT to improve mechanical strength and thermal stability. However, the addition of nitride compounds such as hexagonal boron nitride (h-BN) and aluminum nitride (AlN) into AT has never been reported.

In this research, AT ceramic composites were prepared by conventional reactive sintering at 1500°C for 4 h. The main precursors to synthesis AT were Al₂O₃ and TiO₂. The effect of h-BN and AlN additions content on the phase transition, microstructure, physical properties, mechanical properties, and corrosion behavior of AT ceramics have been systematically investigated.

1.2 Objectives of the study

The main objectives of this research are shown below.

- 1) To investigate the influence of h-BN and AlN addition on phase transition and microstructure of aluminum titanate.
- 2) To investigate the influence of h-BN and AlN addition content on physical properties, mechanical properties, and corrosion resistance of AT composite.

1.3 Scopes of the study

- 1) Study the influence of h-BN and AlN on phase transition and microstructure.
- 2) Characterization of all the prepared AT composites i.e., bulk density, porosity, Thermal expansion coefficient, flexural strength and Vickers hardness.
- 3) Study the corrosion behavior in molten aluminum.

1.4 Benefits of the study

- 1) The stability of the AT composite can be enhanced by the addition of the h-BN and AlN additive.
- 2) Understanding of the emergence of various properties of AT from research.
- 3) The findings of this study can be used to improve the performance and capabilities of future items such as automobile exhaust filters and crucibles

Chapter 2

Theory and literature reviews

2.1 Properties of starting materials

2.1.1 Aluminum oxide (Al_2O_3)

Aluminum oxide (Al_2O_3) or alumina is a compound of aluminum and oxygen with a chemical formula Al_2O_3 . It is the most common form of several aluminum oxides. Al_2O_3 can be found in many phases such as alpha (α), beta (β), and gamma (γ), but the most stable and active phase is the Al_2O_3 in alpha phase. Alpha- Al_2O_3 or corundum has a hexagonal unit cell as shown in Figure 2.1 [18-19]. The oxygen ions arrange in hexagonal closed pack and Al^{3+} ions occupy two thirds of the octahedral sites. The bonding between aluminum and oxygen is very strong, to break this bond, it requires very high energy. The chemical formula of Al_2O_3 therefore rarely changes or has a variety of formulas compared to other oxides. A small amount of the alloy that forms as a secondary phase in the Al_2O_3 structure and has a lower melting point than the Al_2O_3 can cause the melting point of the Al_2O_3 to be lower.

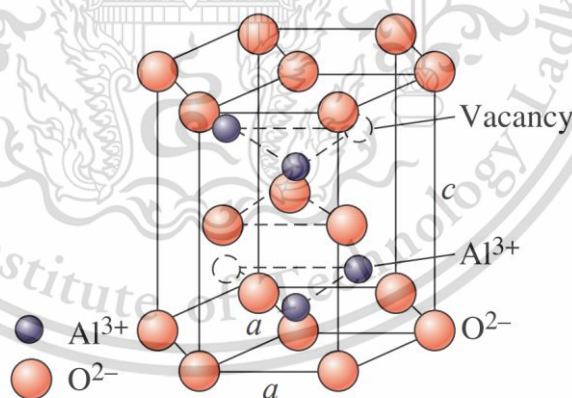


Figure 2.1 Crystal structure of aluminum oxide (Al_2O_3) [20].

Al_2O_3 is an oxide ceramic that has been widely used because of its availability and low cost. Al_2O_3 also has many outstanding properties. The general properties of Al_2O_3 are shown in Table 2.1. Al_2O_3 has high hardness, high abrasion and corrosion resistance, chemical resistance, good high-temperature, and electrical insulation. This material is reserved for educational use only, not allowed for commercial use.

Forbidden to modify the content, and cite the document when use.

Therefore, it can be used in many industrial applications such as abrasive, refractory, paper, and ceramic. Traditional ceramics industrial use natural raw materials containing Al_2O_3 . For advanced ceramics application, synthetic Al_2O_3 can be used to produce many types of products, such as electronic components, auto parts, electrical semiconductors, insulating devices.

Table 2.1 Typical properties of alpha-alumina (Al_2O_3) [19].

Properties	$\alpha\text{-Al}_2\text{O}_3$
Density (g/cm^3)	3–3.98
Melting point ($^\circ\text{C}$)	2004-2096
Flexural strength (MPa)	152-800
Vickers hardness (GPa)	5.5-22
Modulus of elasticity (GPa)	215-413
Thermal conductivity (W/m K)	4.5-10.9

2.1.2 Titanium dioxide (TiO_2)

Titanium dioxide (TiO_2) or titania [21] is also commonly found all over the world. TiO_2 has many unique properties such as high heat resistance, high corrosion resistance, high mechanical strength, and good dielectric properties. TiO_2 can be found in many products including toothbrushes, paper, cosmetics, medical equipment, and electronic parts. Ceramics based on TiO_2 have numerous desirable and potential applications. Their mechanical properties are strongly influenced by composition and microstructure and can thus be tailored. TiO_2 has unique optical properties such as colorless, transparent, and high refractive index which are advantages for optical applications.

TiO_2 has three main crystal structures as shown in Figure 2.3. The first kind is anatase, which has a tetragonal crystal structure and is moderately found in nature. When TiO_2 is heated above $915\text{ }^\circ\text{C}$, the crystal structure changes to rutile which has a tetragonal crystal structure. Rutile structure is the most common TiO_2 found in nature because it is a very stable structure. Rutile also exhibited good dielectric properties and it has a high dielectric constant [22]. The third structure is brookite, which has an orthorhombic crystal structure. Brookite is rarely found in nature. It is stable at low

temperatures. When heated to a temperature above 750 °C, the crystal structure changes to rutile [23].

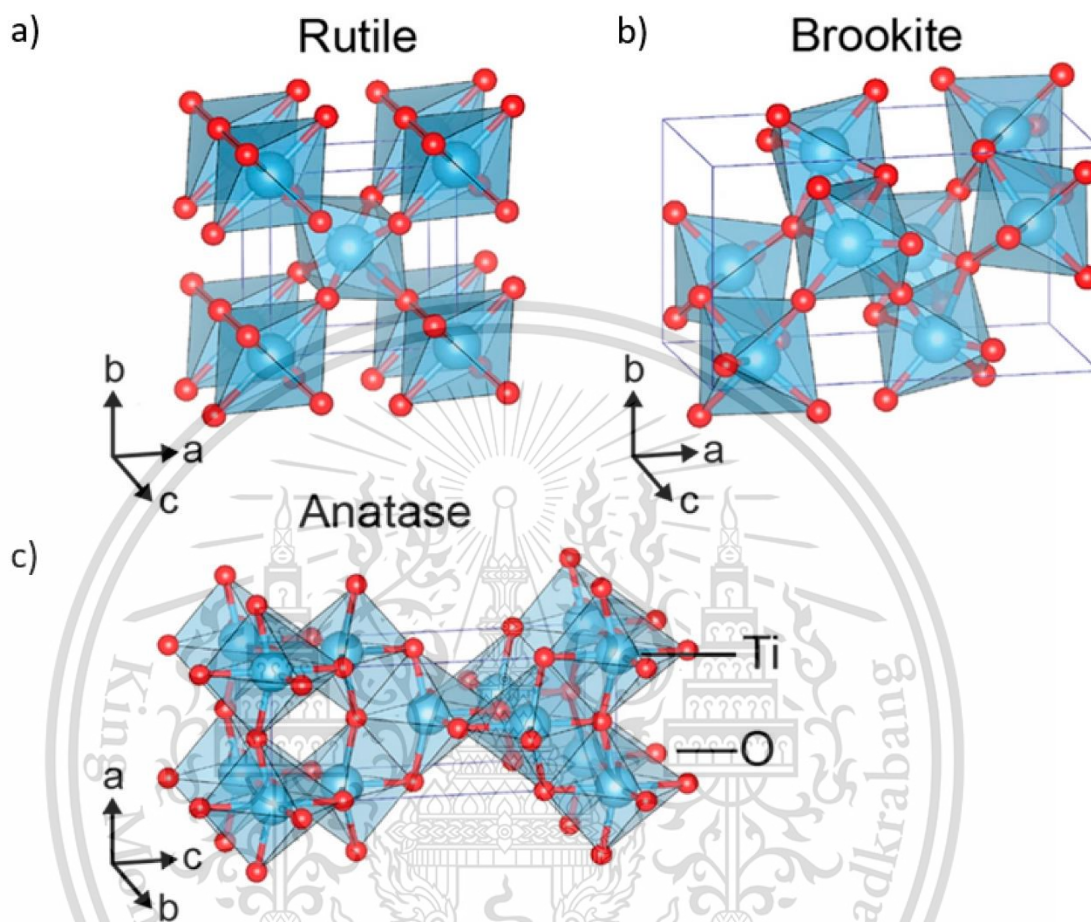


Figure 2.2 Crystal structures of titanium dioxide (TiO₂): (a) rutile; (b) brookite, and (c) anatase [24].

Table 2.2 Properties of titanium dioxide (TiO₂) in different crystal phases.

Structure	Rutile	Anatase	Brookite
Properties			
Crystal structure	Tetragonal	Tetragonal	Orthorhombic
Molecular weight	79.890	79.890	79.890
Density (g/cm ³)	4.2743	3.895	4.123
Specific gravity	3.90 – 4.10	3.90 – 4.10	3.90 – 4.10
Melting point (°C)	1,800 – 1,900	2,500 – 3,000	1,800 – 1,900
Boiling point (°C)	2,500 - 3,000	2,500 - 3,000	2,500 - 3,000

This material is reserved for educational use only, not allowed for commercial use.

Forbidden to modify the content, and cite the document when use.

2.1.3 Hexagonal boron nitride (h-BN)

Boron nitride (BN) is a synthetic III-V compound that was discovered in the early 19th century. Boron nitride is available in a variety of crystal structures including hexagons (h-BN), cubic (c-BN) and wurtzite (w-BN), as well as in amorphous form (a-BN). Hexagonal boron nitride (h-BN) is the most common form. Hexagonal boron nitride is also called white graphite because it has crystal structure similar to the hexagonal carbon lattice in graphite. Nitrogen and boron in hexagonal boron nitride also form hexagonal lattice layers which overlap to form crystals. The crystal parameters are quite similar with high diamagnetic and anisotropy.

Hexagonal boron nitride possesses high thermal conductivity, inertness, and tribological properties, so it is attractive as a lubricant and high-temperature ceramic material. Hexagonal boron nitride has a unique combination of physical and chemical properties that give it wide applications in materials technology for oxide-free high-temperature coatings, superconducting tapes for ultra-high field magnets, electronic packaging, melting metal crucibles, and insulation/dielectrics for electronic products [25].

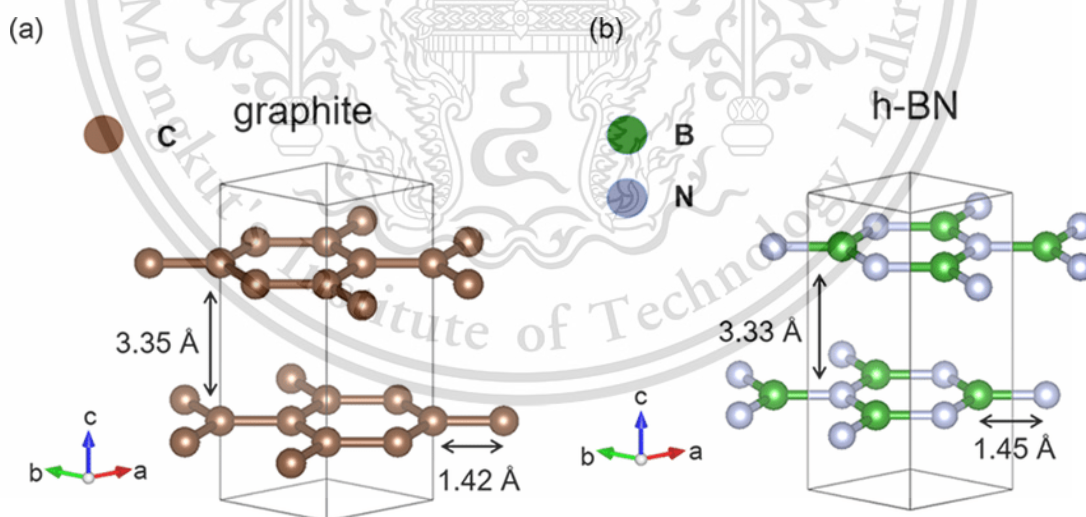


Figure 2.3 Crystal structure of (a) graphite and (b) hexagonal boron nitride (h-BN), taken from [26].

2.1.4 Aluminum nitride (AlN)

Aluminum nitride (AlN) [29] is a covalently bonded ceramic compound that is composed of abundant aluminum and nitrogen elements. It is one of the III–V nontoxic semiconductor materials with a hexagonal structure and thermodynamically stable wurtzite crystal, as shown in Figure 2.4.

Because of its unique combination of properties such as high thermal conductivity, high electrical resistivity, low thermal expansion coefficient, moderately low dielectric constant, good thermal shock resistance, and good corrosion resistance, aluminum nitride (AlN) has been recognized as an important industrial material [27]. It has been considered as a filler for epoxy molding compound (EMC) for microelectronic encapsulation, a substrate for semiconductor chips, and an insulating material for radio frequency and microwave packages. Because of its high thermal conductivity, it has recently been considered for use as a loading substrate for high-power light-emitting diode chips [28]. Despite its many desirable properties, AlN has not yet found widespread application in industry, owing primarily to its high market prices as a result of high production costs. Developing low-cost methods of producing AlN powder is thus an intriguing area of study.

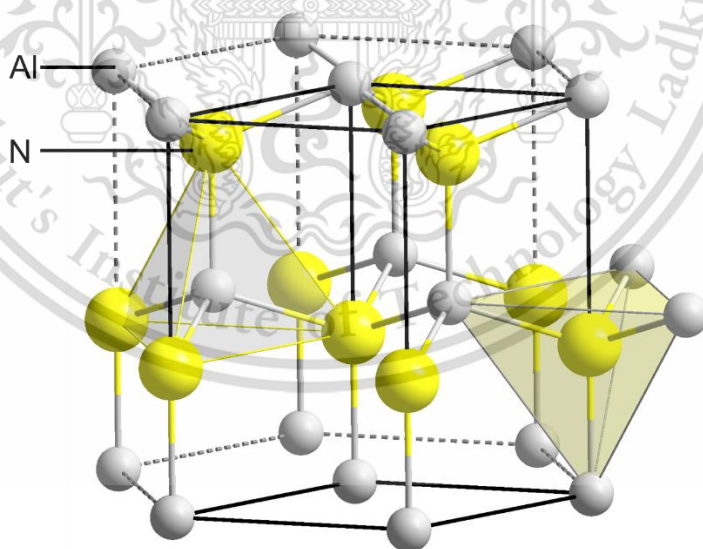


Figure 2.4 Crystal structure of aluminum nitride (AlN) [29].

2.2 Aluminum titanate (Al_2TiO_5 :AT)

2.2.1 Structural, properties, and applications

Aluminum titanate (Al_2TiO_5 or AT) has a mineral pseudo-brookite structure as shown in Fig 2.5. Al_2TiO_5 has an orthorhombic unit cell with a space group $Cmcm(63)$ and the lattice parameters of $a = 3.557 \text{ \AA}$, $b = 9.436 \text{ \AA}$, and $c = 9.648 \text{ \AA}$ [30]. In this structure, each Al^{3+} and Ti^{4+} cation is surrounded by six oxygen ions forming distorted oxygen octahedral. These AlO_6 or TiO_6 octahedra are weakly bonded by shared edges. This crystal structural characteristic is responsible for the high anisotropy of thermal expansion coefficients (-3.0 , $+11.8$ and $21.8 \cdot 10^{-6} \text{ C}^{-1}$, for three crystallographic axes) which generates the internal stresses to cause the microcrack [31]. Al_2TiO_5 is a synthetic ceramic material prepared from Al_2O_3 and TiO_2 at a mole ratio of 1:1. The phase diagram of Al_2O_3 - TiO_2 system is shown in Figure 2.6.

Al_2TiO_5 is a well-known synthetic oxide ceramic material with a high melting point, good refractoriness, non-wetting, resistance to molten aluminum corrosion and has excellent thermal shock resistance due to its relatively low coefficient of thermal expansion and thermal conductivity [6]. Al_2TiO_5 material is now a ceramic with wide-ranging application prospects. The physical properties of Al_2TiO_5 are listed in Table 2.3.

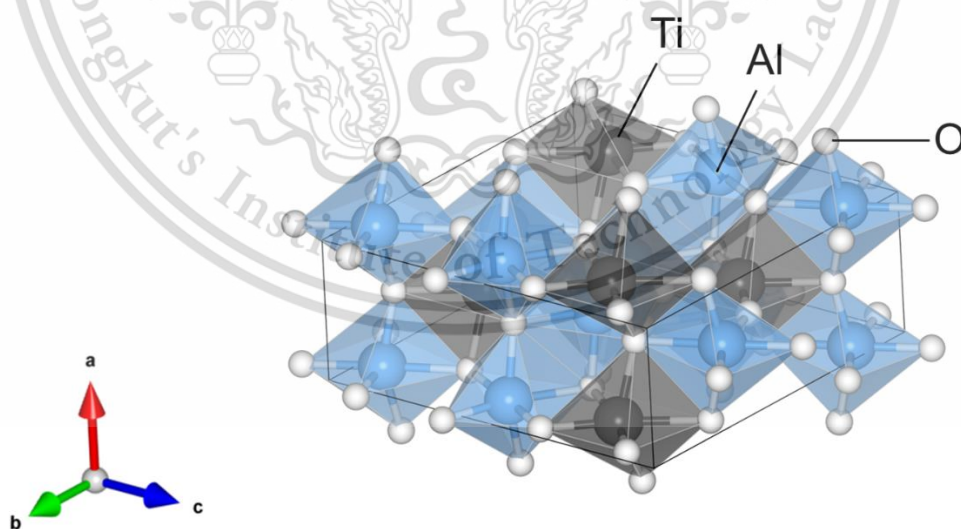


Figure 2.5 Crystal structure of aluminum titanate (Al_2TiO_5).

This material is reserved for educational use only, not allowed for commercial use.

Forbidden to modify the content, and cite the document when use.

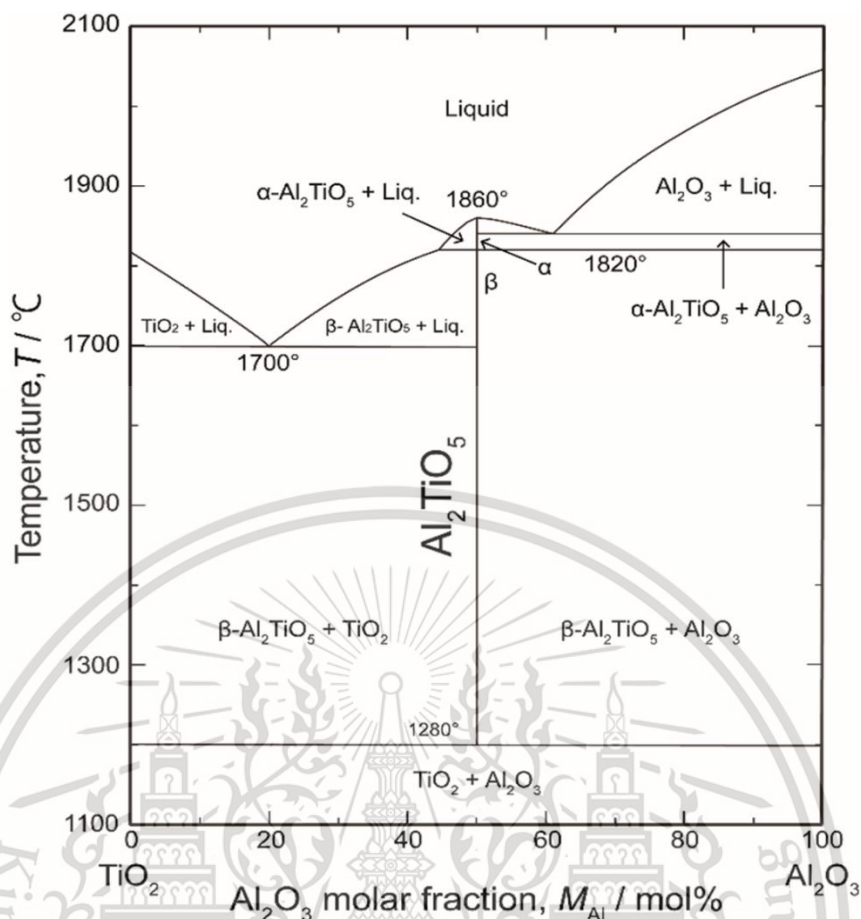


Figure 2.6 Phase diagram of Al_2O_3 - TiO_2 system.

Table 2.3 Typical properties of aluminum titanate (Al_2TiO_5 , AT).

Properties	Al_2TiO_5
Density (g/cm^3)	3.70
Melting point ($^\circ\text{C}$)	1860
Flexural strength (MPa)	5
Hardness (GPa)	4-20
Thermal expansion coefficient average ($\times 10^{-6} \text{ } ^\circ\text{C}^{-1}$)	-0.5-3
Thermal conductivity ($\text{W}/\text{m K}$)	0.9-1.5

This material is reserved for educational use only, not allowed for commercial use.

Forbidden to modify the content, and cite the document when use.

Al_2TiO_5 ceramic materials have a wide range of technological applications, including thermal insulation liners, soot particulate filters in diesel engines, spacing rings of catalytic converters, foundry crucibles, launders, nozzles, riser tubes, pouring spouts, and thermocouples for non-ferrous metallurgy and master molds in the glass industry. The example of Al_2TiO_5 ceramic parts used in industry is shown in Fig 2.7.

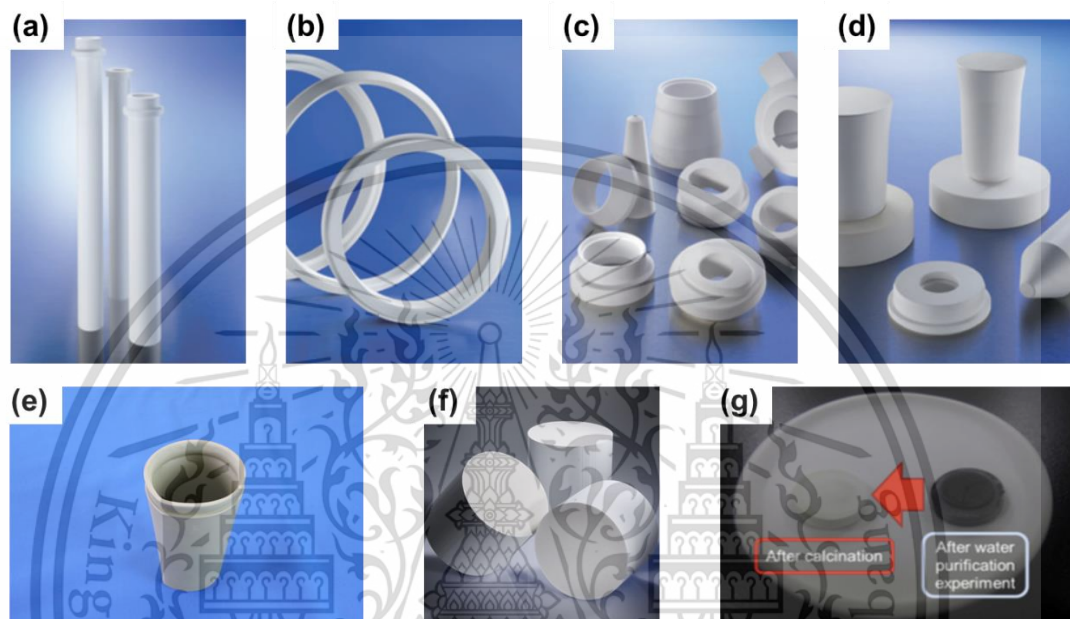


Figure 2.7 Applications of aluminum titanate, (a) riser tubes, (b) breakrings, (c) nozzles/bushes, (d) stopper/plates, (e) diesel particulate filter (DPF) [8], and (f) water filter [32].

2.2.2 Limitation of monolithic aluminum titanate

Monolithic Al_2TiO_5 has some drawbacks that limit its application. There are two main issues. The first issue is that pure Al_2TiO_5 is unstable at temperatures below 1300°C and decomposes into two phases, Al_2O_3 and TiO_2 as shown in equation 2.1, resulting from eutectic reaction.



This decomposition occurs when the adjacent Al^{3+} (0.54 \AA) and Ti^{4+} (0.67 \AA) octahedral collapse because the lattice site occupied by the Al^{3+} ion is too large. The thermal

energy available from such structure disruption collapse allows Al^{3+} to migrate from its position and causes structural dissolution to TiO_2 and Al_2O_3 .

Another issue is that pure Al_2TiO_5 has a low mechanical strength due to the anisotropy of its crystal structure, which promotes a low thermal expansion coefficient and leads to microcracking. This micro-cracking reduces the material's mechanical strength [30].

2.3 Effects of oxide addition on thermal stability and mechanical properties of aluminum titanate

Many researchers have studied to improve the thermal stability and enhance the mechanical properties of Al_2TiO_5 . It is well-known that the thermal stability of Al_2TiO_5 can be improved by forming a solid solution using oxide additives such as MgO and Fe_2O_3 . The substitution of the elements from these oxides at the cation site (Al^{3+} or Ti^{4+} sites) results in the increase in the free energy of thermal decomposition of Al_2TiO_5 .

Thomas et al. [11] investigated the effects of ZrO_2 on the microstructure and properties of Al_2TiO_5 composite by using the reaction sintering technique. The results showed that increasing the mechanical strength of Al_2TiO_5 had a negligible effect on its excellent thermal properties. This was attributed to the formation of extra microcracks because of the ZrO_2 phase transformation and the unusual microstructure produced by the presence of ZrO_2 .

Jiang et al. [12] studied the effects of additives (MgO , SiO_2 , and Fe_2O_3 or their compound additives) on the bulk density, phase composition, mechanical strength, and thermal shock resistance of Al_2TiO_5 that were prepared by reaction sintering ceramics. It was found that additives of MgO , SiO_2 , and Fe_2O_3 or their compounds are favorable to reducing the porosities of Al_2TiO_5 , enhancing mechanical strength and thermal shock resistance. The role of additives can be rationalized in terms of promotion of the sintering process, formation of new phases, and influence on the lattice constant (*c*-axis) of Al_2TiO_5 structure.

Chen et al. [13] reported that additives such as MgO , Fe_2O_3 and their mixture, can be dissolved in Al_2TiO_5 ceramics to promote the formation of elongated grains and grain boundary microcracks. The interlocking microstructure was formed by the

elongated grains, which limited crack propagation. Furthermore, microcracks can provide gaps for grains to relocate, resulting in obvious sample flexibility.

In particular, the Al_2TiO_5 ceramics doped with MgO and Fe_2O_3 (ATFM) show optimum flexibility with a deflection of about 0.55 mm and flexural strength up to 13.85 MPa. On the other hand, the SiO_2 additive can reduce the size of grains and microcracks, resulting in high mechanical strength but poor flexibility. The successful fabrication of such Al_2TiO_5 flexible ceramics will provide potential opportunity for anti-vibration and refractory application.

Oikonomou et al. [14] studied the effect of adding Fe_2O_3 on the stability and properties of Al_2TiO_5 and studied the effect of adding mullite ($3\text{Al}_2\text{O}_3 \cdot 2\text{SiO}_2$) content of 5–50% by weight on the mechanical properties of Al_2TiO_5 . The experiment results showed that Al_2TiO_5 (iron oxide stabilized)–mullite composites had high mechanical strength combined with outstanding thermal stability.

Perera et al. [15] studied the fracture strengths of three Al_2TiO_5 -based materials containing mullite and different thermal stabilizers (Fe_2O_3 and MgO). From the experiment, it was found that mullite acts as a reinforcing phase, increasing the fracture strength with respect to monolithic materials. MgO does not produce a significant change in mechanical properties relative to the undoped material containing mullite. In opposition, Fe_2O_3 induces severe microcracking of the samples, which leads to a noticeable decrease in fracture strength.

Wang et al. [17] developed a two-step sintering technique for porous ceramics to optimize porosity and mechanical strength. The process involves prolonged sintering at low temperatures (T_1) and rapid sintering at higher temperatures (T_2). Porous ceramics of aluminum titanate-strontium feldspar-mullite (ASM) ternary composite were prepared by this technique. The sintered samples with $T_1 = 1400^\circ\text{C}$ and $T_2 = 1500^\circ\text{C}$ had the appropriate porosity and bulk density. The sample showed the thermal expansion coefficient (TEC) of $2.9 \times 10^{-6}/\text{K}$, flexural strength of 9.22 MPa, porosity of 63.48%, bulk density of 1.20 g/cm^3 , and average porosity (D_{50}) of $15.94 \mu\text{m}$. The two-step sintering method produced porous ceramics with excellent properties.

Maki et al. [33] studied Al_2TiO_5 ceramic doped with 0–15 mol% MgO by reactive sintering. It was found that MgO doping was effective in reducing the grain size of the Al_2TiO_5 matrix and reducing the strong anisotropy of Al_2TiO_5 , resulting in fewer cracks.

The maximum strengths of the Al_2TiO_5 sample doped with 15 mol% MgO sintered at 1400 and 1500°C were 106 MPa and 32 MPa, respectively.

According to the literature review, it can be concluded that the role of additives can be rationalized in terms of the promotion of the sintering process and the formation of new phases of Al_2TiO_5 ceramics. Additives such as ZrO_2 , MgO, SiO_2 , and Fe_2O_3 or their compounds are beneficial for reducing the porosities of Al_2TiO_5 and enhancing mechanical strength and thermal shock resistance. For MgO additives, several studies had reported that MgO was effective in reducing the grain size of the Al_2TiO_5 matrix and reducing the strong anisotropy of Al_2TiO_5 , resulting in fewer cracks. Adding a small amount of MgO has also been shown to improve the stability of Al_2TiO_5 .

2.4 Improving of mechanical properties by formation of Al_2TiO_5 composites

Fabrication of Al_2TiO_5 composites with other ceramics is one of the significant ways to enhance phase stability and strength.

Park et al. [34] investigated the effect of starting powder on morphology of and grain growth in an Al_2O_3 - Al_2TiO_5 composite using calcined Al_2O_3 , TiO_2 , and Al_2TiO_5 as starting powder. The study showed that when Al_2O_3 and TiO_2 were used as the starting powders, the morphology of the Al_2O_3 - Al_2TiO_5 composite provides a narrower size distribution and a smaller average grain size of Al_2O_3 than those using Al_2O_3 and Al_2TiO_5 as starting powder.

Bueno et al. [35] used Al_2O_3 and TiO_2 starting powders to fabricate dense and microcrack-free Al_2O_3 / Al_2TiO_5 composites with varying composition at 10, 30, and 40% Al_2TiO_5 content. The starting materials were synthesized by colloidal filtration and then fabricated the composites by reaction sintering. Colloidal filtration of optimized suspensions with solid loadings as high as 50 vol% and sintered at 1450°C resulted in fully reacted and uncracked sintered materials with uniformly distributed Al_2TiO_5 contents of up to 40 vol% with high density. The thermal diffusivity values for the composites at 25–800°C were decreased with temperature and aluminum titanate content.

Meybodi et al. [36] examined the phase composition and microstructure of the Al_2O_3 -20wt% Al_2TiO_5 composite prepared by reaction sintering Al_2O_3 nano-powder and TiO_2 at 1300, 1400, and 1500 °C for 2h. In microstructural analysis, the average grain

size of the $\text{Al}_2\text{O}_3/\text{Al}_2\text{TiO}_5$ composite increased with temperature. SEM also showed a suitable interface between Al_2TiO_5 and Al_2O_3 grains and a distribution of Al_2TiO_5 particles in the grain boundary region. XRD showed no rutile- TiO_2 in the sintered composite, confirming Al_2TiO_5 formation. The samples sintered at 1300°C, 1400°C, and 1500°C had hardness of 4.8 GPa, 6.2 GPa, and 8.5 GPa, respectively.

Al_2TiO_5 materials typically need to choose between having a very low coefficient of thermal expansion and a high mechanical strength. Although the microcracking restricts that strength, it helps to lower the coefficient of thermal expansion. Therefore, the Al_2TiO_5 material is especially resistant to thermal stress. There are now a variety of designs available to increase the strength of Al_2TiO_5 materials without sacrificing their distinctive properties. From the development of solid solutions to the design of ceramic composites. In addition to their more common application as a refractory material, the possibility of using Al_2TiO_5 materials for more advanced engineering applications, which are already under investigation, is increased by the fact that the properties of these materials have been improved.

2.5 Corrosion behavior of AT composites in molten Al

Takana et al. [38] investigated whether these cracks affect material durability, corrosion resistance and high-temperature performance. The experiment examined how grain boundary cracks affect the corrosion of non-doped aluminum titanate (AT) ceramics in molten Al alloy with a small amount of Mg. AT ceramics corrode on sample surfaces in contact and non-contact with the melt and on ceramic interior open grain boundary crack surfaces. Controlling grain size to close molten alloy cracks may improve AT ceramic corrosion resistance, according to the study. AT ceramics' excellent thermal shock resistance and thermal insulation may be due to anisotropic thermal expansion during cooling from their sintering temperature causing grain boundary microcracks.

Chapter 3

Research methodology

This chapter presents the materials, equipment, and methods used in the study. Synthesis of aluminum titanate (Al_2TiO_5 : AT) ceramics by addition of hexagonal boron nitride (h-BN) and aluminum nitride (AlN) as well as characterization of the samples, such as determination of phase transition, microstructure, physical properties, mechanical properties, and corrosion behavior studies of ceramics. The details of each section are described as follows.

3.1 Chemical and equipment

3.1.1 Chemicals

Raw materials and chemicals used in the experiments are shown in Table 3.1

Table 3.1 Raw materials and chemicals used in experiments.

Materials		Company	Purity (%)	Particle Size (μm)	Density (g/cm^3)
Precursors	Al_2O_3	Nippon light metal	99.0%	1 μm	3.95
	TiO_2	Alfa-Aesar	95.5%	1-2 μm	4.23
Additives	MgO	Fujifilm wako chemical	99.9%	0.2 μm	3.58
	h-BN	TanYun chemicals	99.0%	10 μm	2.10
	AlN	Sigma-Aldrich	>98%	<100 nm	3.26
Mixing media	Ethanol	RCI Labscan	96%	-	0.790

This material is reserved for educational use only, not allowed for commercial use.

Forbidden to modify the content, and cite the document when use.

3.1.2 Tools and equipment

Tools and equipment used in the experiment are shown in Table 3.2

Table 3.2 Tools and equipment used in experiment

Tools and equipment	Company	Model
Analytical balance 4 digits	Denver Instrument	SI-234
Spatula stainless	-	-
Beakers	-	-
Zirconia balls	-	-
Polypropylene bottle	-	-
Ball-milling machine	-	-
Hot air oven	Memmert	UN55
Sieve 200 mesh	Sanpo	PVC Frame Sieve
Hydraulic pressure	ENERPAC	IPH1240
Vernier caliper	Mitutoyo	Series 500
Alumina crucible	-	-
High temperature furnace	Protherm	PTF 16/75/610
Ultrasonic machine	Bandelin	DT 100H
Density kit	OHAUS	PX224 (Pioneer)
Grinder and polisher machine	Laizhou lyric testing equipment	MP-1C
X-ray Diffractometer (XRD)	Rigaku	MIniflex600
Scanning electron microscope	Zeiss	EVO MA 10
Universal testing machine	Instron	No. 8872
Microhardness tester	Akashi corporation	HM-113

This material is reserved for educational use only, not allowed for commercial use.

Forbidden to modify the content, and cite the document when use.

3.2 Experimental procedure

3.2.1 Preparation of AT/h-BN composite samples

In this experiment, the amounts of raw materials and additives used in the synthesis of AT/h-BN composites were calculated by the stoichiometry technique. Raw materials and additives used for preparing the composition mixtures are listed in Table 3.1. To synthesis AT ceramic, two raw materials were applied: alumina (Al_2O_3) and titania (TiO_2). Magnesium oxide (MgO) was used as an additive to stabilize the structure of AT. Hexagonal boron nitride (h-BN) was applied to improve the mechanical properties of AT.

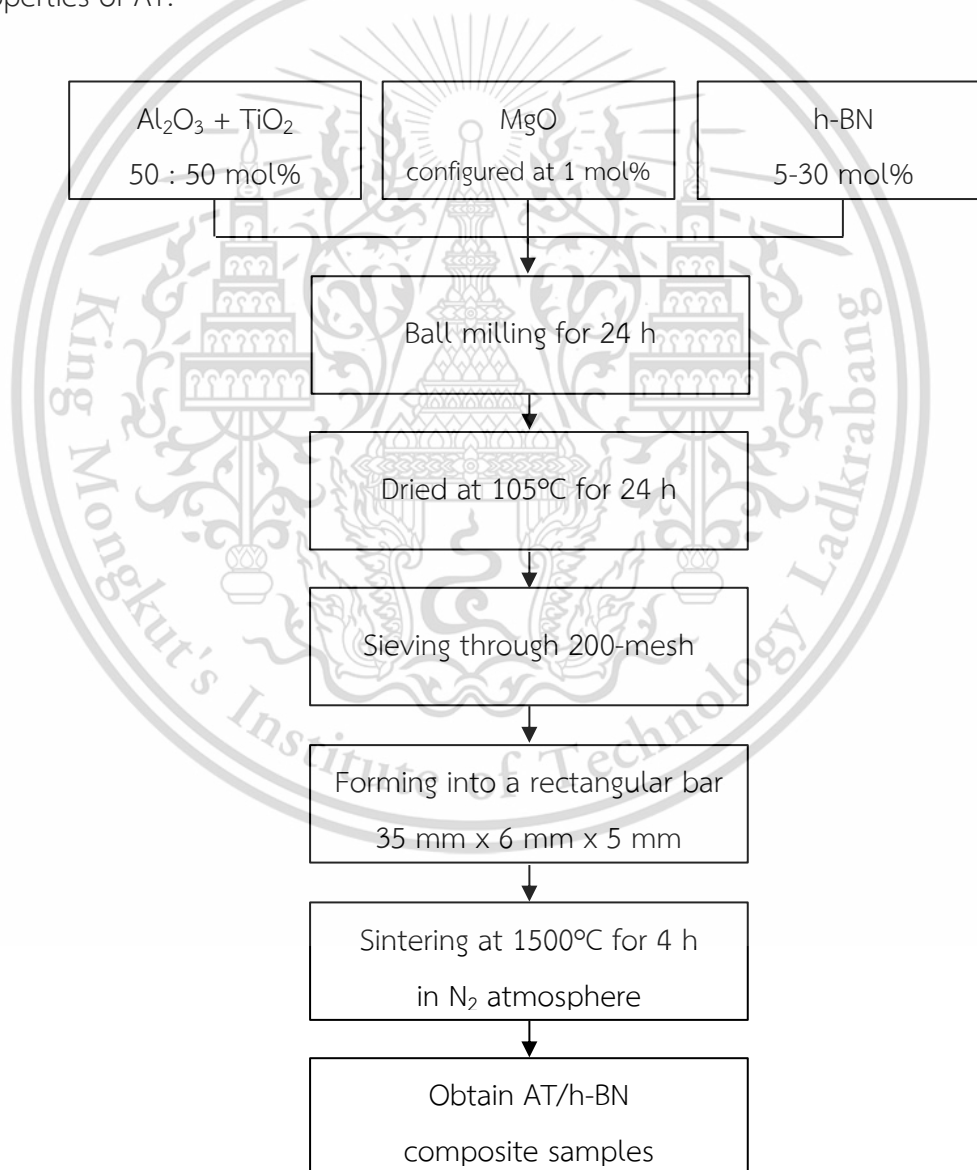


Figure 3.1 Schematic of the preparation of AT/h-BN composite samples.

The flow chart diagram in Figure 3.1 illustrates the AT/h-BN composite sample preparation procedure. Each step of sample preparation can be described as follows:

- 1) All starting materials were weighed by an electronic balance to the relative proportions of each substance calculated in Table 3.3
- 2) After weighing, poured the powder into a polypropylene bottle for wet mixing for 24 h at 300 rpm by using a ZrO_2 ball as the grinding medium and ethanol as a mixing media.
- 3) The mixture slurry was then filtered into a beaker and dried in the oven to remove the ethanol at $105^\circ C$ for 24 h.
- 4) The dried mixture powder was sieved through a 200-mesh sieve.
- 5) The mixed powder was put into a stainless-steel mold and then uniaxially pressed with a hydraulic press at 40 MPa to produce a sample with dimension of 35 mm x 6 mm x 5 mm as shown in Figure 3.2.
- 6) The green samples were put into an alumina crucible using boron nitride powder as an embedded powder.
- 7) The samples were sintered by a high-temperature furnace as shown in Figure 3.3 at $1500^\circ C$ with a heating rate of $5^\circ C/min$. After 4 h of holding time, cooled down to room temperature at a cooling speed of $5^\circ C/min$. Figure 3.4 shows the heating profile for sintering AT composites.
- 8) After sintering, the samples were ultrasonically cleaned in DI water and dried at $105^\circ C$ for testing.

Table 3.3 Compositions of the starting powders used for AT/h-BN composite

Condition no.	Sample ID	Content (mol%)			
		Al_2O_3	TiO_2	MgO	h-BN
1	AT	49.5	49.5	1	0
2	ATBN5	47	47	1	5
3	ATBN10	44.5	44.5	1	10
4	ATBN15	42	42	1	15
5	ATBN20	39.5	39.5	1	20
6	ATBN30	34.5	34.5	1	30

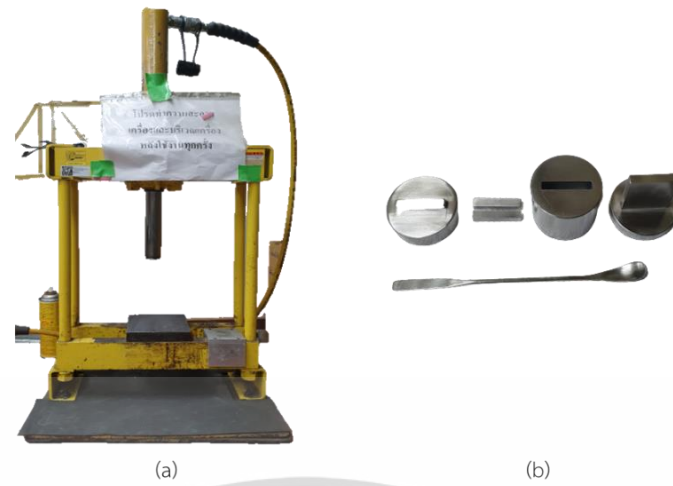


Figure 3.2 (a) Hydraulic pressing machine (IPH1240, ENERPAC), and (b) set of molds used in the forming process.

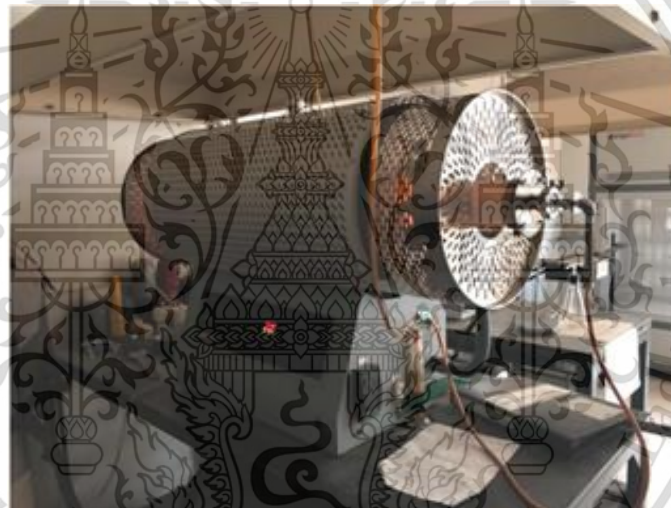


Figure 3.3 High-temperature furnace machine

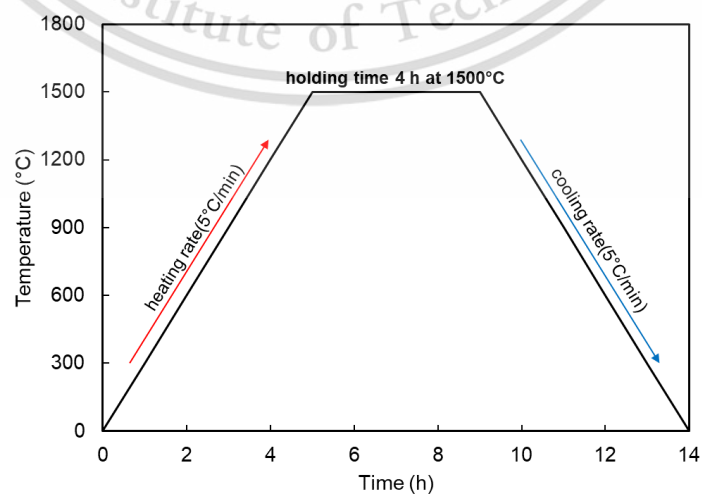


Figure 3.4 The heating profile for sintering AT composites.

This material is reserved for educational use only, not allowed for commercial use.

Forbidden to modify the content, and cite the document when use.

3.2.2 Preparation of AT/AlN composite samples

To synthesize AT/AlN, all starting materials were weighed on an electronic balance according to the calculated relative proportions of each substance in Table 3.4 and then mixed by the wet mixing method for 24 h at 300 rpm using ZrO₂ balls as the grinding medium and ethanol as the mixing medium. It was then dried at 105°C for 24 h and then sieved through a 200-mesh sieve to obtain the ceramic powder of the AT/AlN composite then formed by pressing the pellets into rectangular bars, size 35 mm x 6 mm x 5 mm, with a stainless-steel mold by using a hydraulic press at a pressure of approximately 40 MPa and then the sample were sintered at 1500°C for 4 h with a heating and cooling rate of 5°C/min in N₂ atmosphere.

Table 3.4 Compositions of the starting powders used for AT/AlN composite

Condition no.	Sample ID	Content (mol%)			
		Al ₂ O ₃	TiO ₂	MgO	AlN
1	A30TN	19.5	59.5	1	20
2	A40TN	29.5	49.5	1	20
3	A50TN	39.5	39.5	1	20

3.3 Sample characterization

In this section, the AT/h-BN and AT/AlN composite ceramic samples produced in Sections 3.2.1 and 3.2.2 were subjected to characterization and property assessment. X-ray diffraction patterns (XRD) were employed to identify the material phases, while scanning electron microscopy (SEM) was used to observe microstructures. A wide range of properties, encompassing physical, mechanical, thermal, and chemical aspects, were examined. Figure 3.5 provides an overview of the sequential steps involved in characterizations and property measurements.

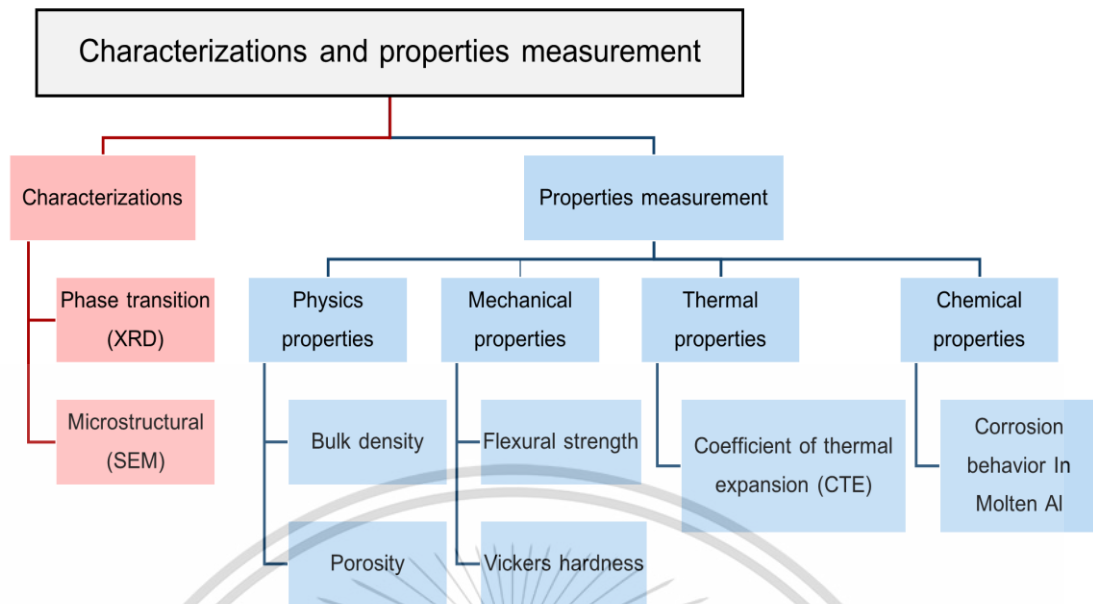


Figure 3.5 Flow chart of characterizations and properties measurements.

3.3.1 Phase composition analysis by XRD

The phase composition and transition of the sintered sample were examined using the X-ray diffraction (XRD) technique. Figure 3.6 displays the XRD equipment (Miniflex600, Rigaku) utilized in this study. The preparation of sample and testing are as follows.

- 1) The sample was prepared by packing finely ground sintered powder into a sample holder, then smoothing the top surface of the material.
- 2) The sample was placed in the sample holder inside the XRD machine.
- 3) The investigation condition was set according to Table 3.5.
- 4) The X-ray diffraction data of the samples was analyzed by comparing the data that was collected with the data in the powder diffraction file (PDF file) using the PDXL2 program.

Table 3.5 Measurement parameters for X-ray diffraction phase analysis.

Item	Condition
X-ray source	CuK α
Start angle (deg.)	10
Stop angle (deg.)	80
Step angle	0.02



Figure 3.6 X-ray diffractometer (XRD).

3.3.2 Densification analysis

The bulk density and porosity of sintered samples were examined using the Archimedes method in accordance with ASTM C373-88. The experimental schematic of Archimedes method and weighing scale for measuring Archimedes are shown in Figures 3.7 and 3.8, respectively. The sample preparation and testing process are as follows.

- 1) The samples were boiled in DI water for 6 h.
- 2) After cooling to room temperature, the sample was immersed in deionized water for 24 h.
- 3) The weight of the samples while suspended in water was weighted and recorded as the "suspended weight" (*S*).
- 4) The samples were then blotted with the damp cloth before being weighed in the air and recorded as the "saturated weight" (*M*).
- 5) The samples were then dried in an oven at 105 °C for 24 h.
- 6) The samples were left to the room temperature then weighed and recorded as dry weight (*D*).
- 7) The bulk density (g/cm^3) was calculated by equation 3.1.
- 8) The porosity (%) was calculated by equation 3.2.

Bulk Density,
$$\rho_b = \frac{D}{M - S} \quad (3.1)$$

Porosity,
$$P = \left(\frac{\rho_a - \rho_b}{\rho_b} \right) \times 100 \quad (3.2)$$



Fig 3.7 Weighing Scale for measuring Archimedes.

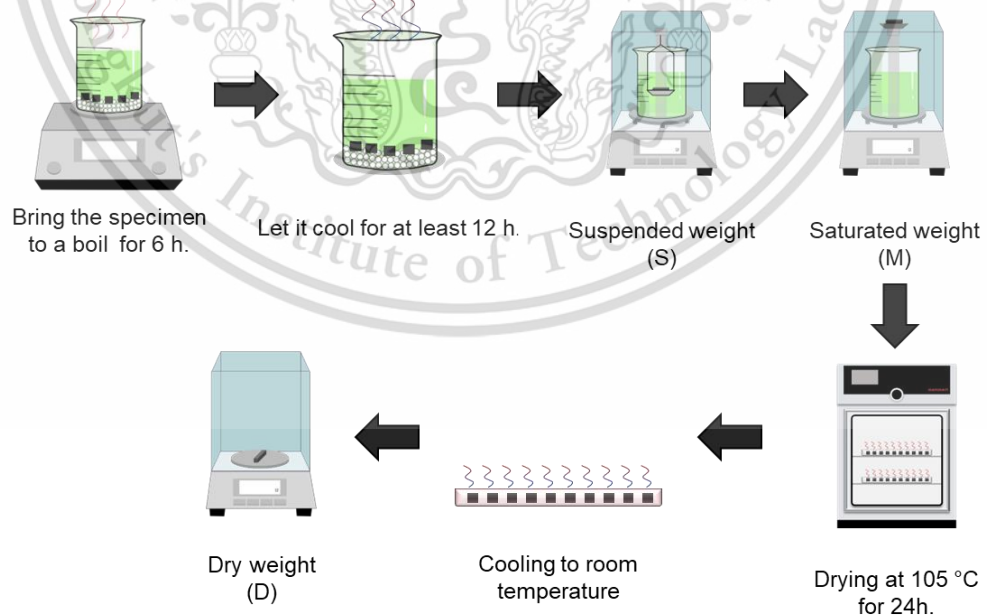


Figure 3.8 The experimental schematic of Archimedes' method.

This material is reserved for educational use only, not allowed for commercial use.

Forbidden to modify the content, and cite the document when use.

3.3.3 Microstructural and chemical analysis

The microstructures of all samples were examined using scanning electron microscopy (SEM) combined with energy dispersive X-ray spectroscopy (EDX) by a Zeiss EVO MA10, as shown in Figure 3.9. The sample has been polished with diamonds of varying sizes and finished with a 1 mm diamond using a grinder and polisher machine (MP-1C, Laizhou Lyric), then cleaned by ultrasonic waves and dried in an oven to remove moisture. Then coated the surface with gold (Au) to make the sample conduct electricity.



Figure 3.9 Scanning electron microscopy (SEM).

3.3.4 Flexural strength analysis

The flexural strength of the sintered samples was examined by the three-point bending test technique using a universal testing machine (No.8872, Instron) as shown in Figure 3.10. The sample preparation and procedure are in accordance with ASTM D790. The procedure for preparing and testing the sample is as follows.

In this test, five samples were used for each measurement to determine the average flexural strength of the sample.

- 1) The sample was cut into rectangular bars measuring 4 mm x 3 mm x 35 mm (width x height x length \pm 0.13 mm).

- 2) Then, the sample is polished with sandpaper, in order of sanding from coarse to fine sandpaper.
- 3) The sample was then ultrasonically cleaned and dried in an oven at 105 °C for 24 h to remove moisture.
- 4) The sample is placed on the supporting jig. The distance between the support legs (L) is set at 20 mm, as shown in Figure 3.11.
- 5) At the start of the test, the sample is gradually pressed by the load pin or crosshead at a speed of 1.0 mm/min.
- 6) When the tested sample is pressed until it breaks, record the braking load (F).
- 7) The bending strength of the sample was calculated using Equation 3.3.
- 8) After calculating the bending strength of the first sample, the remaining samples are further tested according to steps 1-4.

$$\sigma = \frac{3FL}{2bh^2} \quad (3.3)$$

Where: σ is the bending strength (MPa)

F is the braking load (N)

L is the distance between two support pins (mm)

b is the width of samples

h is the thickness of samples



Figure 3.10 Universal testing machine.

This material is reserved for educational use only, not allowed for commercial use.

Forbidden to modify the content, and cite the document when use.

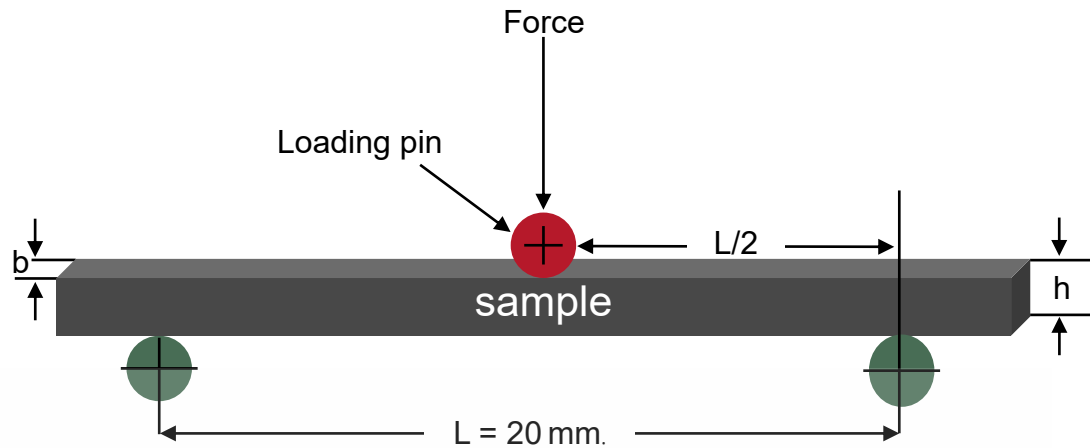


Figure 3.11 Schematic of the 3-point flexural strength test.

3.3.5 Hardness analysis

Sintered samples are polished to obtain mirror surface for indentation testing. The hardness test was carried out using a Vickers hardness tester (HM-113, Mitutoyo) as shown in Figure 3.12. The procedure for testing the sample is as follows.

- 1) The polished sample is placed on the test bench.
- 2) The sample stand is moved up until the surface of the sample is clearly displayed on the microscope screen.
- 3) A diamond pyramid indenter presses on the surface of the sample with a weight of 1 kg and holds for 10 s.
- 4) After 10 s, the diamond pyramid indenter is lifted. The sample was then measured for the diagonal lengths of the indentations (d_1 and d_2) as shown in Figure 3.12, and the mean value D was calculated.
- 5) The hardness value of each sample was calculated using Equation 3.4.
- 6) Samples are subjected to the hardness test according to steps 1-4 at least 10 points to calculate the average value.

$$HV = 1.854 \left(\frac{F}{d^2} \right) \quad (3.4)$$

Where: HV is the Hardness number of samples (Kg/mm^2),

F is the applied force (Kg)

d is the diagonal's average length (mm)

This material is reserved for educational use only, not allowed for commercial use.

Forbidden to modify the content, and cite the document when use.



Figure 3.12 Vickers Hardness Testing Machine.

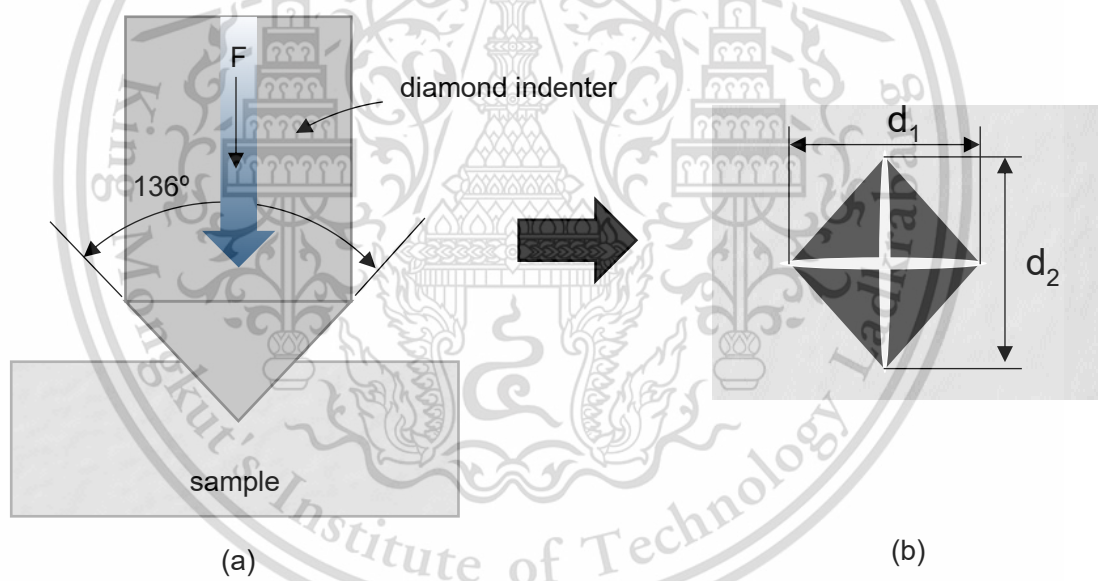


Figure 3.13 (a) schematic operation principles of the Vickers hardness machine and (b) the measurement of impression diagonals.

3.3.6 Coefficient of thermal expansion (CTE)

All sintered composite samples are measured for thermal expansion using a Dilatometer (L76, Kinetics Corporation Ltd.) as shown in Figure 3.14. The temperature used for testing is in the range of 25-1000°C at a heating rate is 5°C/min.

This material is reserved for educational use only, not allowed for commercial use.

Forbidden to modify the content, and cite the document when use.

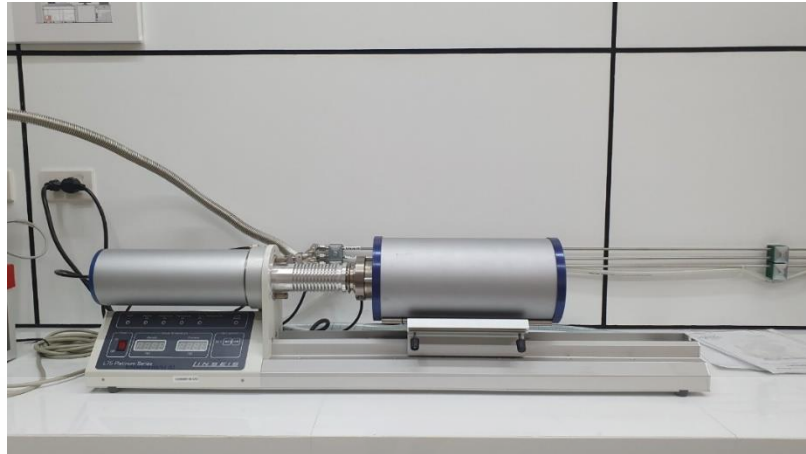


Figure 3.14 Dilatometer used to measure CTE of all composite samples.

3.3.7 Corrosion in molten aluminum test

The corrosion behavior of all sintered samples in molten aluminum was investigated using the immersion corrosion testing method. The aluminum ingot used in this study is the ADC 12 alloy, and its chemical composition is shown in Table 3.6. Figure 3.15 depicts the experimental setup for an immersion test in molten Al. For each soaking test, approximately 300 g of pure Al are melted in an alumina crucible, and a K-type thermocouple is covered with a closed-ended alumina tube. Immerse it in liquid Al to measure the temperature.

Samples for each condition were immersed separately in molten aluminum at 720 °C for durations of 4, 24, and 48 h. After completing the designated immersion period, the samples were removed and air-cooled. Subsequently, the samples were embedded in resin utilizing a Metallurgical mounting press machine (SimpliMet 2, Buehler), as demonstrated in Figure 3.16. The cross-sectional surfaces were then polished for SEM examination.

Table 3.6 Chemical composition (in wt.%) of ADC 12 alloy.

Element	Al	Si	Cu	Fe	Zn	Cr	Mn	Mg	Ni
wt.%	84.8	10.5	2.33	0.864	0.637	0.389	0.233	0.221	0.0759

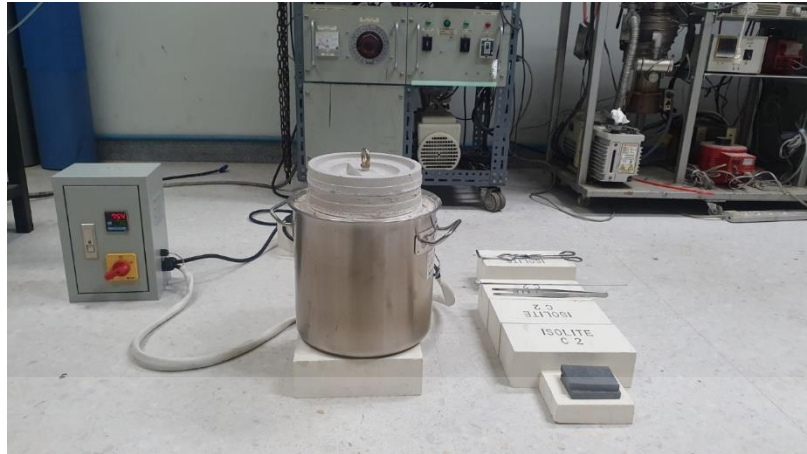


Figure 3.15 The experimental setup for an immersion test in molten Al.



Figure 3.16 Metallurgical mounting press machine.

Chapter 4

Results and Discussion

In this chapter, the experimental results are divided into two main sections. The first section discusses the effect of h-BN additives on the properties of AT composites. The second section focuses on the influence of AlN additions on both the properties and corrosion behavior of AT composites in molten aluminum.

4.1 AT composites with h-BN addition (ATBN composites)

4.1.1 Phase transition analysis (XRD)

The X-ray diffraction (XRD) patterns of sintered AT and ATBN composites with different amounts of h-BN are shown in Figure 4.1. The XRD analysis of all samples revealed the presence of aluminum borate ($\text{Al}_{18}\text{B}_4\text{O}_{33}$; PDF 00-032-0003; space group Amam(63), orthorhombic structure), Al_2TiO_5 or AT (PDF 01-070-1435; space group Bbmm(63), orthorhombic structure), and Al_2O_3 (PDF 01-076-7774; space group R-3c(167), trigonal structure). However, no significant peaks corresponding to h-BN were detected at 26° [11]. Moreover, with an increase in the amount of h-BN, the peak intensity of both $\text{Al}_{18}\text{B}_4\text{O}_{33}$ and Al_2O_3 phases was found to increase, while the peak intensity of Al_2TiO_5 decreased.

The formation of $\text{Al}_{18}\text{B}_4\text{O}_{33}$ typically involves the reaction of Al_2O_3 and B_2O_3 as shown in Eq 4.3 at high temperatures in a solid-state reaction. It is possible that during the initial reaction, the reduction of TiO_2 resulted in the release of oxygen (as shown in Eq 4.1) [12], which could have reacted with h-BN and oxidized it to form B_2O_3 (as shown in Eq 4.2) [13]. Due to the consumption of TiO_2 during the initial step, the reaction between TiO_2 and Al_2O_3 was retarded as shown in Eq 4.4, leading to a reduction in the formation of Al_2TiO_5 . As a result, there was an increase in the formation of $\text{Al}_{18}\text{B}_4\text{O}_{33}$ and a corresponding decrease in the formation of Al_2TiO_5 , which was observed in the final composite. It is noticed that $\text{Al}_{18}\text{B}_4\text{O}_{33}$ was also formed in the AT specimen, despite the initial powder did not contain h-BN. This phenomenon could be explained by the possibility that the starting powder reacted with h-BN, which was used as the embedded powder.

This material is reserved for educational use only, not allowed for commercial use.

Forbidden to modify the content, and cite the document when use.

$\text{Al}_{18}\text{B}_4\text{O}_{33}$ is a compound with complex crystal structure and unique properties, such as high hardness, high melting point, and excellent thermal stability. These properties therefore significantly affect the properties of Al_2TiO_5 composites. The XRD analysis also revealed a shift of the peak position of Al_2TiO_5 towards the lower angle, which could indicate a possible solid solution in the lattice structure. The formation of a solid solution in the composite could potentially lead to improved mechanical properties due to the altered crystal structure and resulting microstructure. However, additional analyses are needed to verify the presence of a solid solution and its potential impact on the properties of the composite.

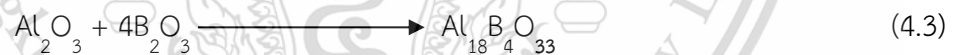
1. Possible Reduction of TiO_2 :



2. Oxidation of h-BN by Released Oxygen:



3. Formation of $\text{Al}_{18}\text{B}_4\text{O}_{33}$:



4. Retardation of TiO_2 and Al_2O_3 reaction



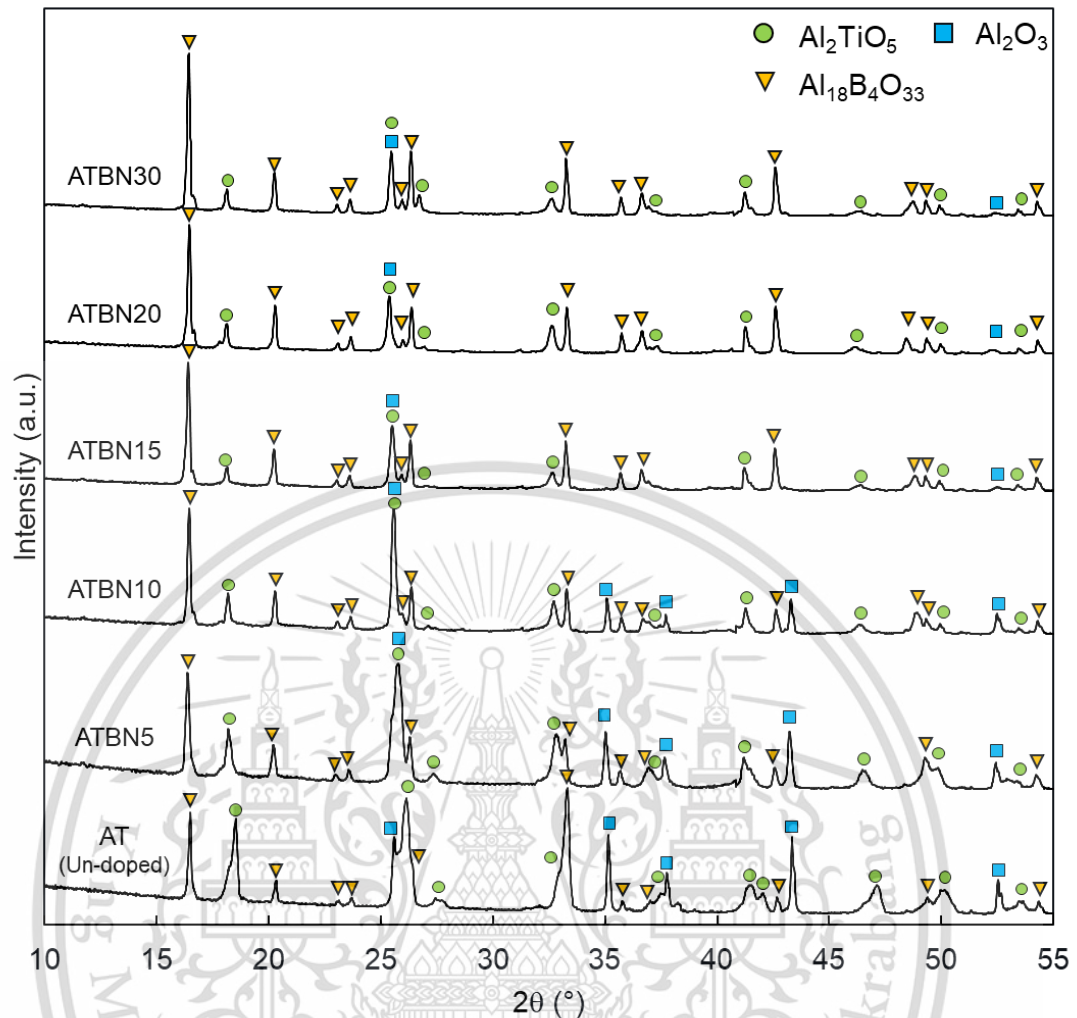


Figure 4.1 The XRD patterns of sintered AT and ATBN composites.

4.1.2 Physical properties (bulk density and porosity)

After the sintering process of the AT/h-BN composite ceramic samples at 1500°C for 4 h, a density test was performed. The bulk density and porosity of the composite were determined using the Archimedes method, according to the ASTM C373-88 standard. This procedure included immersing the samples in boiling water for 6 h and allowing them to soak for an additional 24 h before weighing them. Table 4.1 displays the bulk density and porosity values for each composite, while Figure 4.2 presents a graphical summary of the data, employing the same variables.

The figure illustrates the correlation between bulk density and porosity of the composite as the h-BN addition increased from 0 to 30 mol%. As the amount of h-BN added increased, there was a gradual rise in bulk density. The composites without

h-BN (AT sample) exhibited the lowest bulk density of 2.70 g/cm^3 , whereas the composites with 20 mol% h-BN (ATBN20) demonstrated the highest bulk density of 3.12 g/cm^3 . Subsequently, the bulk density declined significantly as the h-BN content increased to 30 mol%, yielding a density value of 2.71 g/cm^3 .

Conversely, the porosity of the composite exhibited an inverse trend with bulk density. The AT sample exhibited the highest porosity of 25.98% while increasing the h-BN amount led to a decrease in the porosity of the ATBN composite. The lowest porosity value of 2.75% was observed for the ATBN20 composite. Meanwhile, the Porosity value of ATBN30 rose to 23.91%.

In this study, the addition of h-BN and the subsequent reaction sintering likely played a significant role in promoting the densification of the composites. As the h-BN content increased, it reacted with the other starting materials, which promoted the formation of solid phases $\text{Al}_{18}\text{B}_4\text{O}_{33}$ and Al_2TiO_5 and released heat. The heat generated by the exothermic reactions then caused the particles to consolidate and densify, thus contributing to the densification of the composites. In addition, the densification of the composites can also be attributed to the elimination of pores and defects during reaction sintering. This mechanism of densification through reaction sintering could further improve the strength and hardness of the composites.

Table 4.1 Bulk density and porosity of samples.

Sample ID	Bulk density (g/cm^3)	Porosity (%)
AT	2.70 ± 0.04	25.98 ± 1.34
ATBN5	2.76 ± 0.06	22.29 ± 1.32
ATBN10	2.79 ± 0.04	18.24 ± 1.15
ATBN15	2.84 ± 0.16	11.38 ± 1.54
ATBN20	3.12 ± 0.04	2.75 ± 1.14
ATBN30	2.71 ± 0.09	23.91 ± 1.48

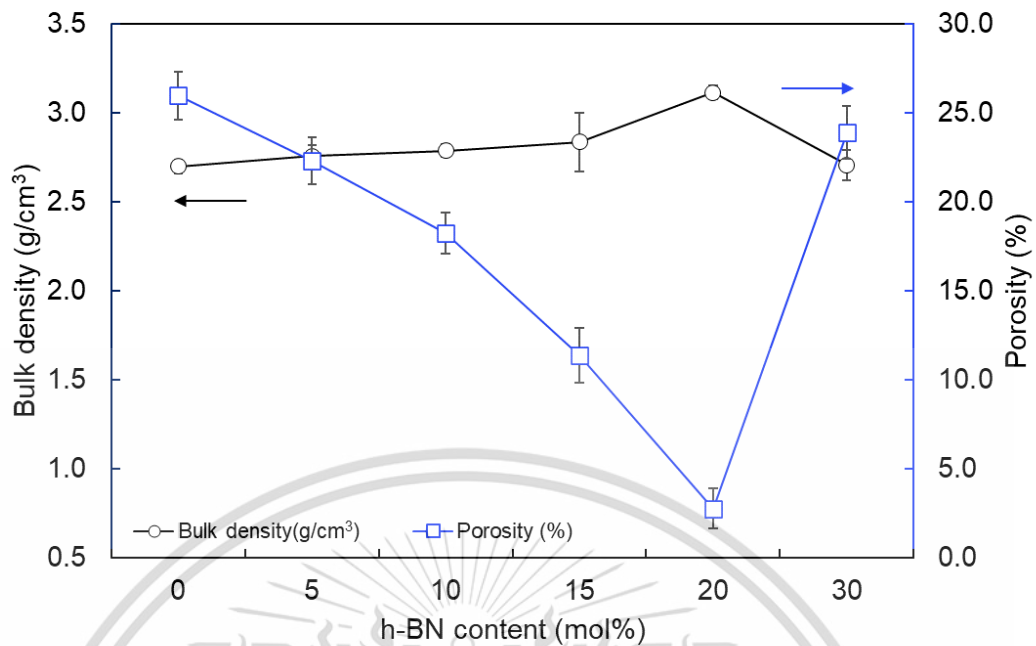


Figure 4.2 The bulk density (black graph) and porosity (blue graph) of samples with different h-BN content.

4.1.3 Microstructure and chemical analysis (BSE-SEM)

The polished surface of AT and ATBN composites was observed using backscattered electron scanning electron microscopy (BSE-SEM) as presented in Figure 4.3. The SEM images showed the presence of both dark and bright phases that were homogeneously distributed throughout composites. However, further investigation is required to accurately identify and verify the composition of each phase. It can be observed that the addition of h-BN to the composite led to a reduction in the number of large pores which is consistent with the porosity results discussed earlier. Furthermore, when observed a high magnification image at the dark area (inset image), the number of small pores also decreased significantly. This suggests that the addition of h-BN to the composite not only reduced the number of large pores but also resulted in the elimination of small pores within the microstructure. The elimination of pores and defects during reaction sintering can further contribute to the improved mechanical properties of the composite.

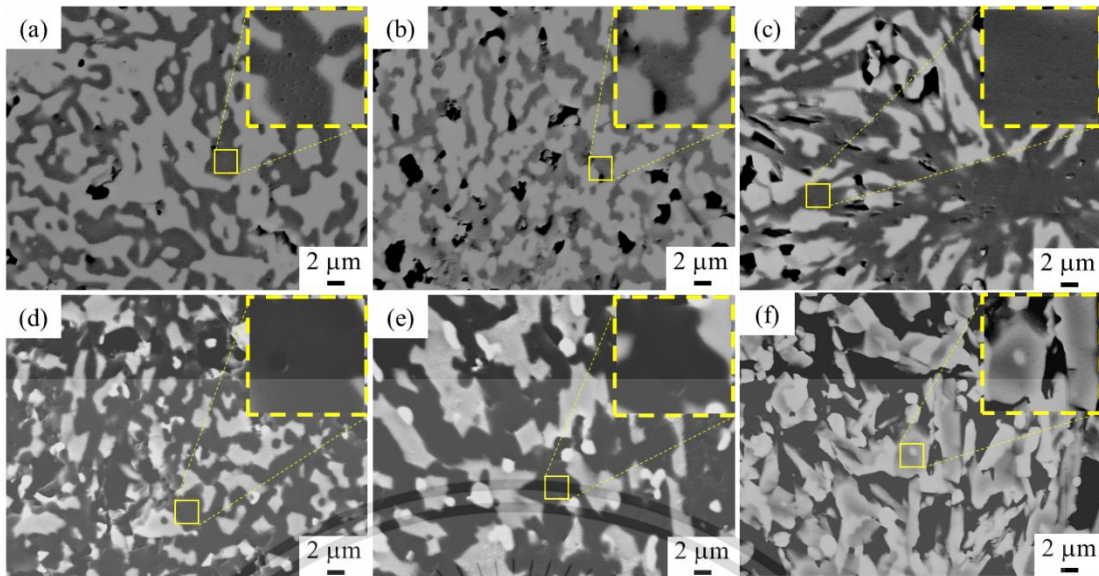


Figure 4.3 BSE-SEM images of polished surface of (a) AT, (b) ATBN5, (c) ATBN10, (d) ATBN15, (e) ATBN20, and (f) ATBN30. The inset image in each figure represents a high magnification of a rectangular area.

4.1.4 Mechanical properties (Flexural strength and Vickers hardness)

Figure 4.4 displays the effect of h-BN content on the flexural strength of AT and ATBN composites. The results indicate that the flexural strength of the composite significantly increased as the content of h-BN was increased. The flexural strength of AT composites was 13.7 MPa. The highest flexural strength, reaching 123.6 MPa, was achieved with ATBN20. However, as the h-BN content was increased to 30 mol%, the flexural strength decreased to 30 MPa.

Figure 4.5 illustrates the effect of h-BN content on the Vickers hardness of the composites. The results demonstrate an increase in Vickers hardness from 5.6 GPa to 11.2 GPa as the h-BN content was increased from 0% to 20% and then gradually decreases to 6.02 GPa with increasing h-BN content to 30 mol% (ATBN30).

These results are consistent with physical properties examination, which showed increased bulk density and decreased porosity as the amount of h-BN was increased. This improvement in mechanical properties can be attributed to the densification of the composites as a result of the reaction sintering process, which reduced the amount of porosity. The present study demonstrated that the incorporation of h-BN in the AT composites led to the formation of $Al_{18}B_4O_{33}$ and an

enhanced reaction sintering process, resulting in significant improvements in the mechanical properties of the composites.

It has been noted in previous studies that an excessive content of $Al_{18}B_4O_{33}$ has the potential to diminish the flexural strength [37]. This is consistent with the findings of our study, in which the addition of 30 mol% h-BN resulted in an excess of the $Al_{18}B_4O_{33}$ phase. Consequently, this excess phase led to a decrease in the mechanical properties.

The increased density, decreased porosity, and homogeneous microstructure also played a significant role in achieving the high strength Al_2TiO_5 composites. These properties make it useful in a variety of applications, such as in the production of refractory materials and structural ceramics components.

Table 4.2 Flexural strength and Vickers hardness of samples.

Composition	Flexural strength (MPa)	Vickers hardness (GPa)
AT	13.68 ± 4.02	5.61 ± 1.85
ATBN5	43.08 ± 8.40	7.84 ± 1.96
ATBN10	49.76 ± 14.58	8.01 ± 2.44
ATBN15	54.75 ± 7.55	9.90 ± 1.11
ATBN20	123.62 ± 8.91	11.15 ± 4.11
ATBN30	30.04 ± 3.22	6.02 ± 2.03

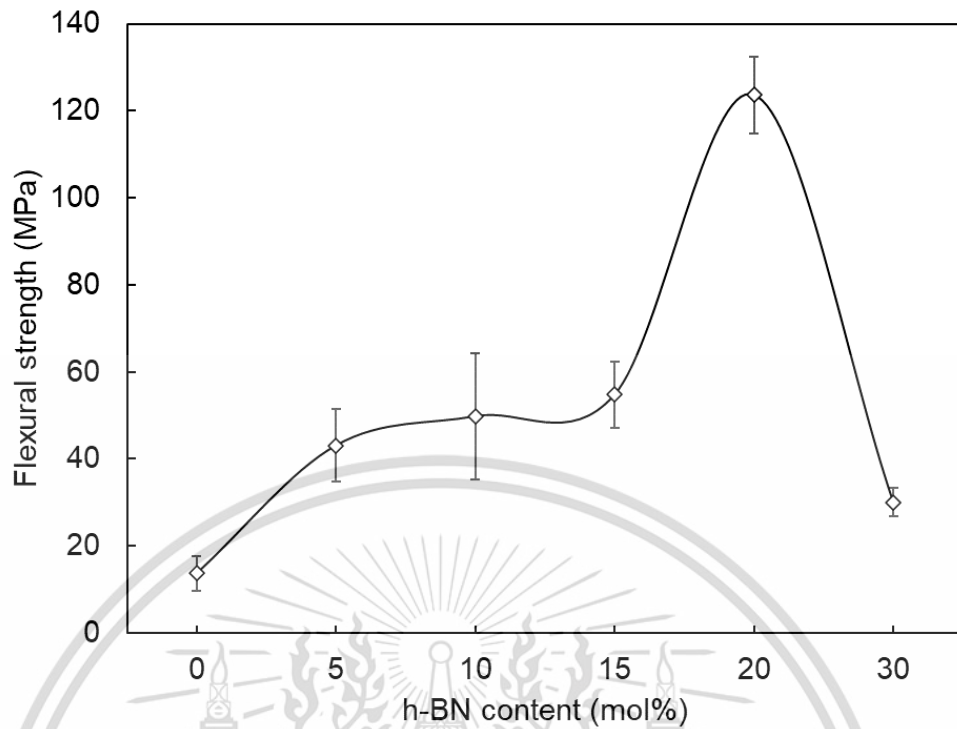


Figure 4.4 The effect of h-BN content on the flexural strength of Al_2TiO_5 composites.

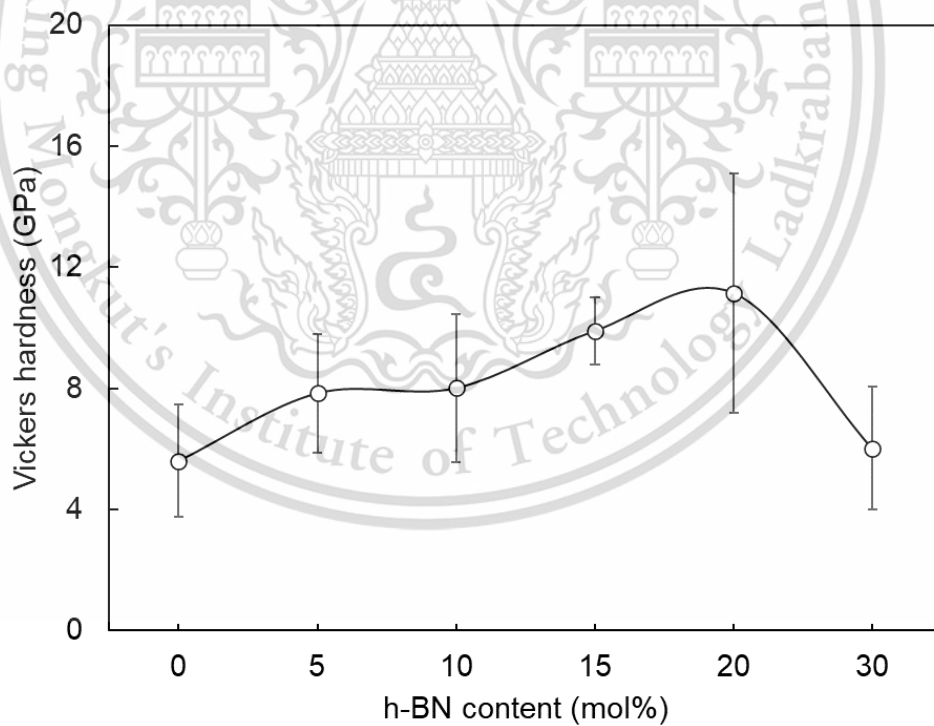


Figure 4.5 The effect of h-BN content on the Vickers hardness of Al_2TiO_5 composites.

4.1.5 Thermal properties (CTE)

Figure 4.6 shows a graph of the relationship between temperature and the thermal expansion of the sample. From the graph, it can be concluded that the thermal expansion of the ATBN sample increases rather rapidly. according to the temperature increase. However, we noticed that ATBN20 still has a low expansion value of about 1.45×10^{-6} in the temperature range not exceeding 400°C . Therefore, if it is used at a temperature that is not very high, that is, in the range not exceeding 400°C , it should be usable. But if the temperature is too high, it will see more expansion. Therefore, we believe that ATBN composites are not suitable for use with molten aluminum. Because it will cause too much expansion. Because the test or use of liquid al will be in the range of $600\text{--}800^\circ\text{C}$, in this part, we didn't take it to test for corrosion further.

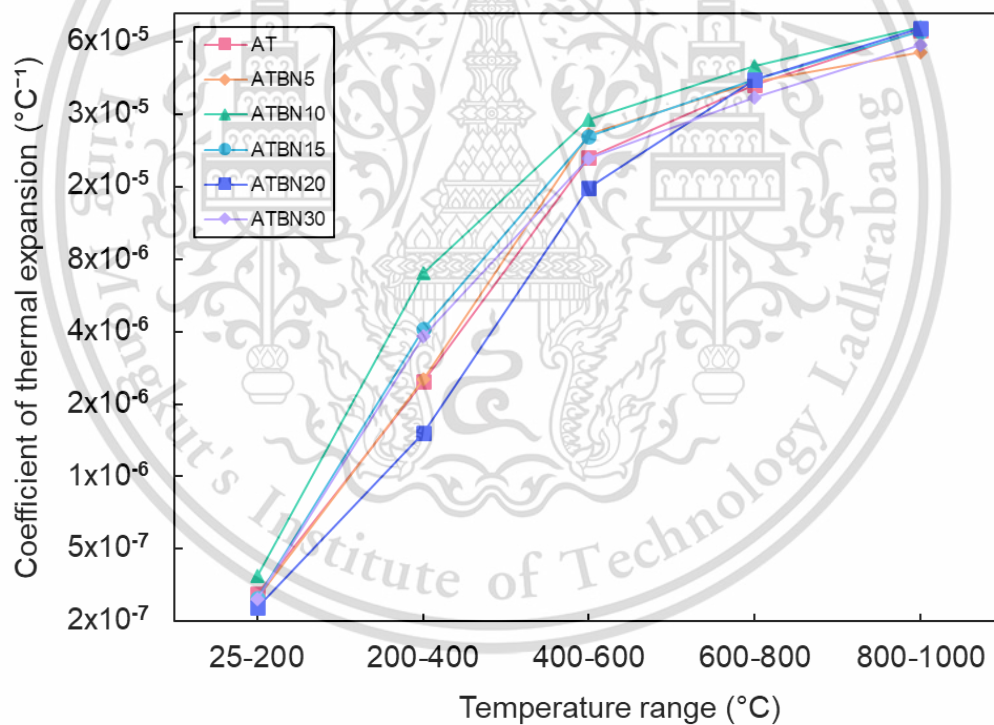


Figure 4.6 The effect of h-BN content on the CTE of Al_2TiO_5 composites.

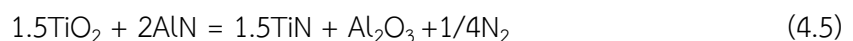
4.2 AT composite with AlN addition

For this study, we changed the additive from h-BN to AlN and set the AlN content at 20 mol% because previous studies [40] found that adding 20 mol% of AlN brought the physical and mechanical properties of the samples within limits. Meanwhile, the XRD results still show high AT peaks, as do the results from the first study. It leads us to conclude that perhaps the amount of Al₂O₃ was too much for the formation of the Al₂TiO₅ phase, so we tried to adjust the amount of Al₂O₃ precursor from the original limit of 50 mol% down to 30, 40, and 50 mol% to compare the results and, upon verification, Various features The results are divided into the following points:

4.2.1 Phase transition analysis (XRD)

The phase transition of the sample was examined by X-ray diffraction (XRD) testing, with the results presented in Figure 4.7. The XRD peaks reveal the presence of Al₂TiO₅ and AT as the primary phases, with the Al₂TiO₅ phase exhibiting the highest peak intensity within the composites. Moreover, when the Al₂O₃ precursor was introduced, a noticeable effect on the XRD pattern was observed. Specifically, the peak associated with the Al₂O₃ phase exhibited a slight increase, while the peak related to the Al₂TiO₅ phase showed a gradual decrease. This suggests that the addition of the Al₂O₃ precursor had an impact on the relative proportions of these phases, leading to the peak intensity in the XRD pattern.

Furthermore, the presence of the TiN phase was consistently observed in all the specimens. This observation can be attributed to a reaction between AlN and TiO₂, resulting in the formation of TiN and Al₂O₃, as supported by previous research (as shown in Eq 4.5) [38]. It is important to highlight that TiN is a high-strength nitride compound. Its incorporation into the composite structure has a significant and positive influence on the overall strength of the composite sample. Therefore, the emergence of the TiN phase further enhances the mechanical properties of the material.



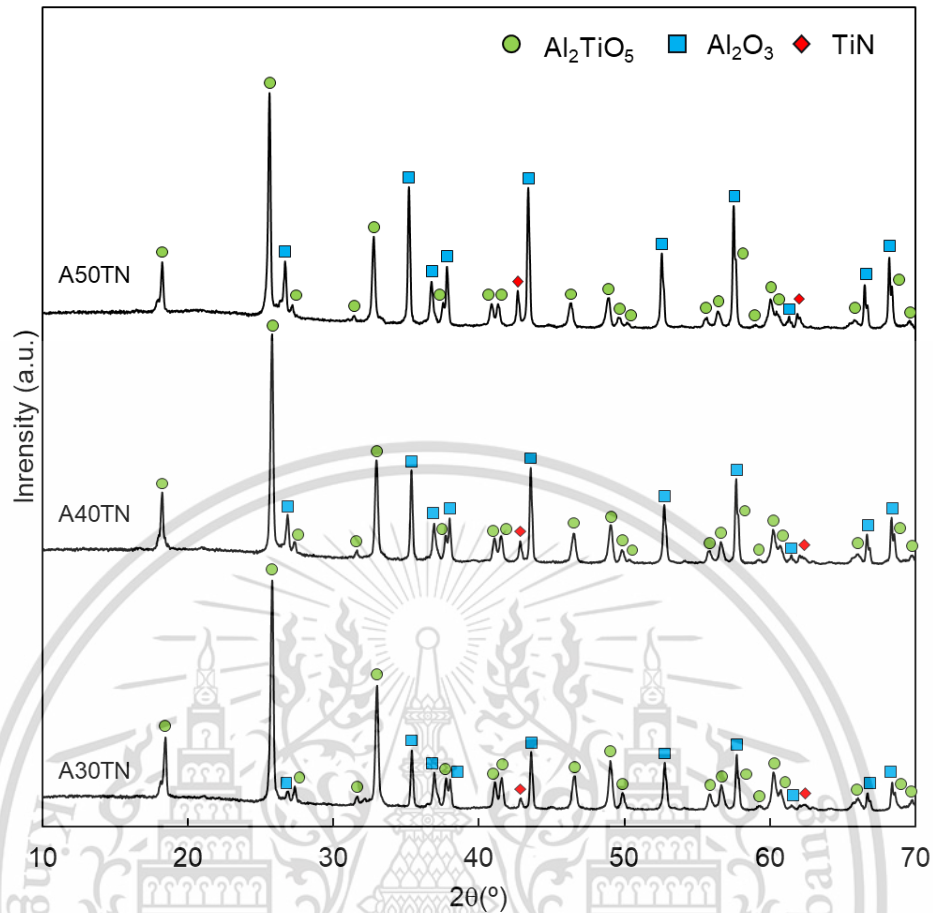


Figure 4.7 X-ray diffraction patterns of samples with different Al_2O_3 content.

4.2.2 Physical properties (bulk density and porosity)

Figure 4.8 displays the bulk density and porosity of the AT composite, where 20 mol% AlN was added with varying Al_2O_3 content, and the corresponding values are shown in Table 4.3. In comparison to the bulk density of AT composites with hBN doping (ranging from 2.70 to 3.12 g/cm^3), the incorporation of AlN significantly increases the bulk density of composites (between 3.79 and 3.91 g/cm^3). This density increase can be attributed to the formation of high-density Al_2O_3 and TiN phases, resulting from the addition of AlN.

Moreover, an increase in the Al_2O_3 precursor content also correlates with a rise in the bulk density of the AT composite. This observed trend indicates that Al_2O_3 precursors play a role in enhancing the density of the composites. This trend suggests that Al_2O_3 precursors play a role in increasing the density of composites. The

investigation revealed that the composite material containing a 30 mol% Al_2O_3 precursor content (A30TN) exhibited a bulk density of 3.79 g/cm^3 . Notably, this bulk density exhibited a gradual increment when the Al_2O_3 precursor content was modified to 40 mol% (A40TN) and 50 mol% (A50TN), resulting in bulk densities of 3.89 g/cm^3 and 3.91 g/cm^3 , respectively. Among these, A50TN displayed the highest bulk density.

On the contrary, the porosity of the AT composite exhibited an opposite trend to the bulk density. In other words, as the bulk density increased, the porosity decreased. This suggests that there is an inverse relationship between the density of the composite material and its porosity. The porosity values for different composites are as follows: A30TN exhibits a porosity of 0.82%, A40TN has a porosity of 0.79%, and A50TN demonstrates the lowest porosity at 0.75%.

These findings align with the earlier XRD results, indicating that as Al_2O_3 content increases, the peaks associated with the Al_2O_3 phase become more prominent, while the peaks related to the AT phase gradually diminish with increasing Al_2O_3 content. This suggests that the presence of the Al_2O_3 phase has a direct impact on the phase composition of the composite material. The formation of high-density phases like Al_2O_3 and TiN correlates with the observed increase in bulk density.

Table 4.3 Bulk density and porosity of samples.

Sample ID	Bulk density (g/cm^3)	Porosity (%)
A30TN	3.79 ± 0.04	0.91 ± 0.27
A40TN	3.89 ± 0.02	0.75 ± 0.26
A50TN	3.91 ± 0.02	0.73 ± 0.24

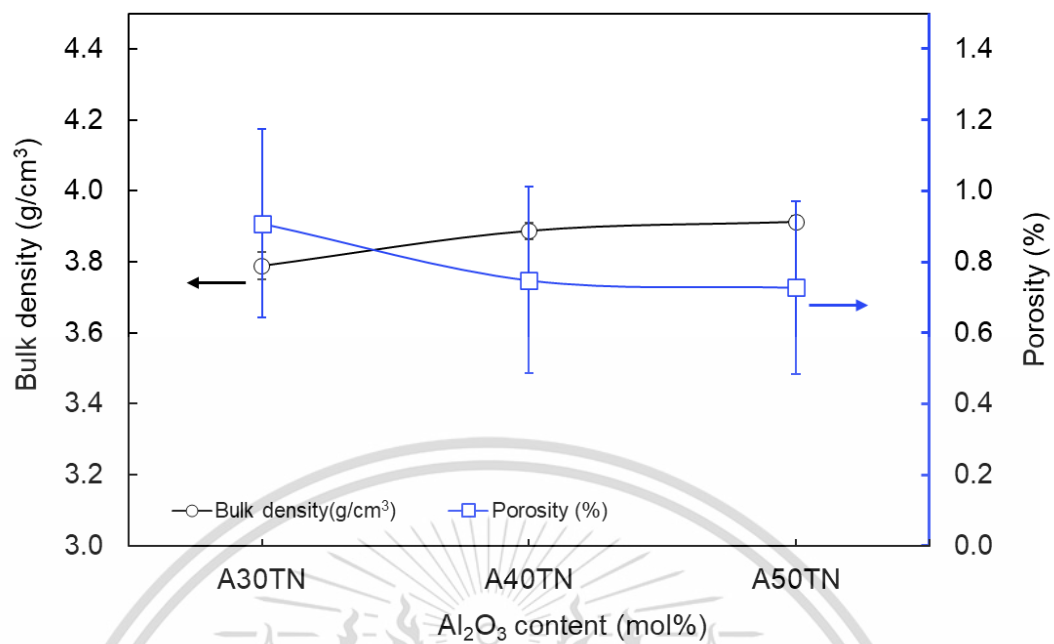


Figure 4.8 The bulk density (black line) and porosity (blue line) of samples with different Al₂O₃ content.

4.2.3 Microstructure (EPMA and BSE-SEM)

The microstructural characteristics of AT composites with different Al₂O₃ precursor contents were investigated on the polished composite surface using scanning electron microscopy (SEM). In this study, the microstructure and chemical composition of A30TN sample were analyzed using EBSD mapping, as depicted in Figure 4.9. The image reveals a prominent black phase rich in both Al and O, leading to the assumption that it represents the Al₂O₃ phase. The light gray phase can be seen to have additional elements, including Al, Ti, O, and a little N. Therefore, this one is expected to be an Al₂TiO₅ phase, but based on the ratio found, it may not be stoichiometric aluminum titanate, but it can be estimated that this light gray phase is Al₂TiO₅ with N added as a solid solution. The quantitative analysis of the composition of the white phase was thought to be the TiN phase, but due to its very small size, signs of O were also found.

Then, when BSE-SEM images of all three samples are compared, as shown in Figure 4.10, the composite material mainly consists of black grains (Al₂O₃), while the light gray phase (Al₂TiO₅) is distributed evenly throughout the specimen. It was observed that when the content of Al₂O₃ in the reactants increased, the area covered

by the black phase also increased. In addition, a smaller white (TiN) phase, measuring less than 1 μm , was distributed throughout the specimen. especially when the amount of Al_2O_3 in the reactant increases. These white phases are, therefore, more pronounced and widespread.

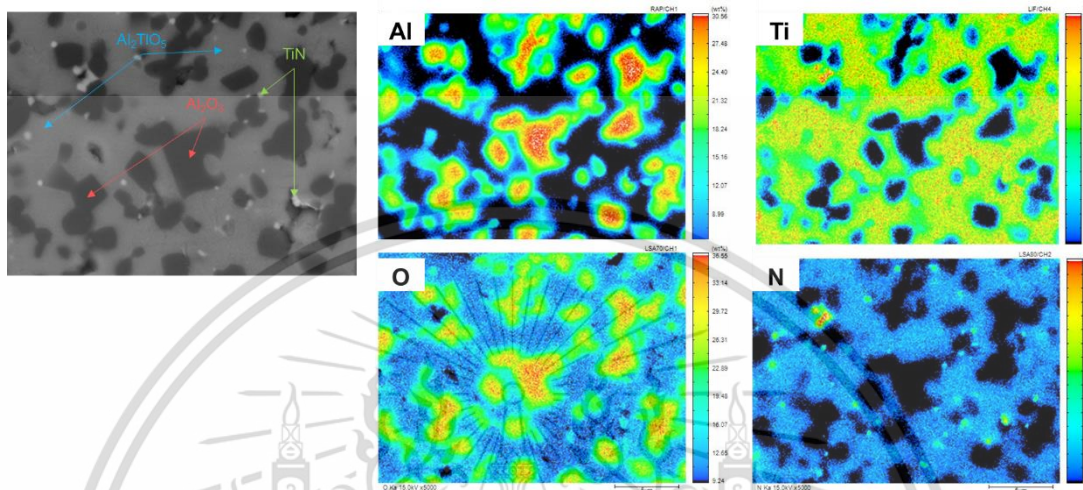


Figure 4.9 EBSD-SEM micrograph of A30TN sample.

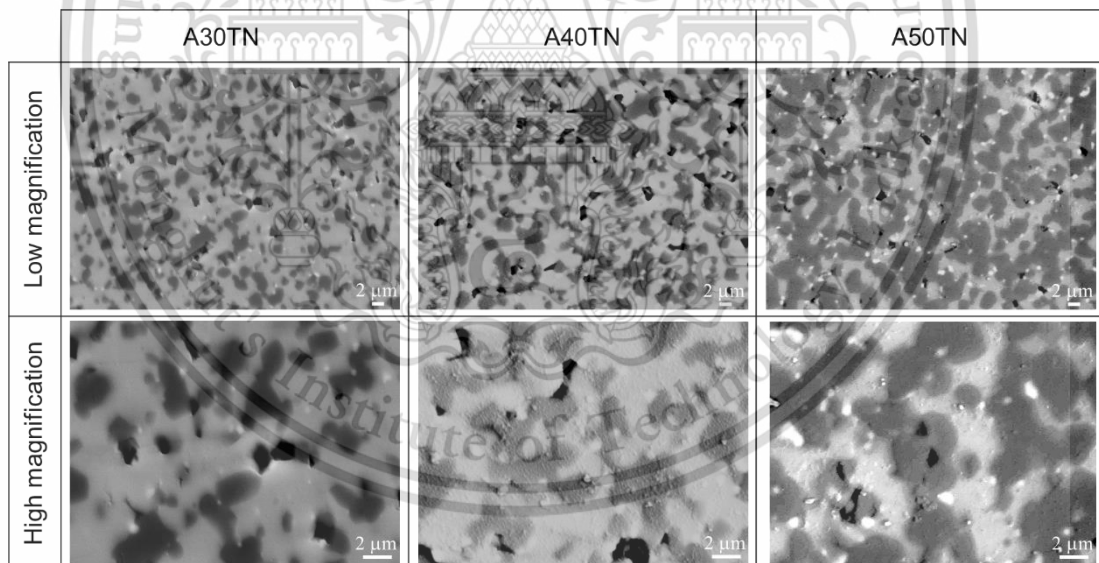


Figure 4.10 BSE-SEM micrograph of samples with different Al_2O_3 content.

4.2.4 Mechanical properties (Flexural strength and Vickers hardness)

The flexural strength and Vickers hardness (H_v) of the AT/AlN composites were measured so that the effects of adding AlN and changing the Al_2O_3 content on the composites could be studied. These factors were found to influence both the phase composition and the strength of the workpiece. The results of both tests are presented in Table 4.4, while Figure 4.10 illustrates the flexural strength and Vickers hardness (H_v) of the composite material.

The flexural strength, represented by the black line, demonstrated a direct correlation with the amount of Al_2O_3 in the composite material. As the mol% of Al_2O_3 precursor increased, the strength also exhibited a gradual increase. Specifically, the composite with 30 mol% Al_2O_3 content (A30TN), achieved a flexural strength of 210.30 MPa. With higher Al_2O_3 content, specifically, at 40 mol% (A40TN) and 50 mol% (A50TN), the flexural strength exhibited a substantial increase, reaching values of 216.87 MPa and 249.12 MPa, respectively.

Similarly, the Vickers hardness value (indicated by the blue line) of the composite from the experimental results showed that the Vickers hardness increased significantly, with A30TN, A40TN, and A50TN composites having values of 11.15 GPa, 11.65 GPa, and 12.87 GPa, respectively.

These findings related to strength, obtained through experiments, align with the results stemming from X-ray diffraction (XRD), scanning electron microscopy (SEM), and various physical properties like bulk density and porosity, as previously discussed. The presence of greater amounts of Al_2O_3 and TiN phases, accentuated by an increase in the Al_2O_3 precursor content and the addition of AlN, is closely related to the enhanced strength characteristics of the composite material. This suggests that the composition and phase transitions in the composite play a significant impact on its mechanical properties.

Table 4.4 Flexural strength and Vickers hardness of samples.

Composition	Flexural strength (MPa)	Vickers hardness (GPa)
A30TN	210.30 ± 21.51	11.15 ± 0.57
A40TN	216.87 ± 16.94	11.65 ± 0.85
A50TN	249.12 ± 28.70	12.87 ± 1.49

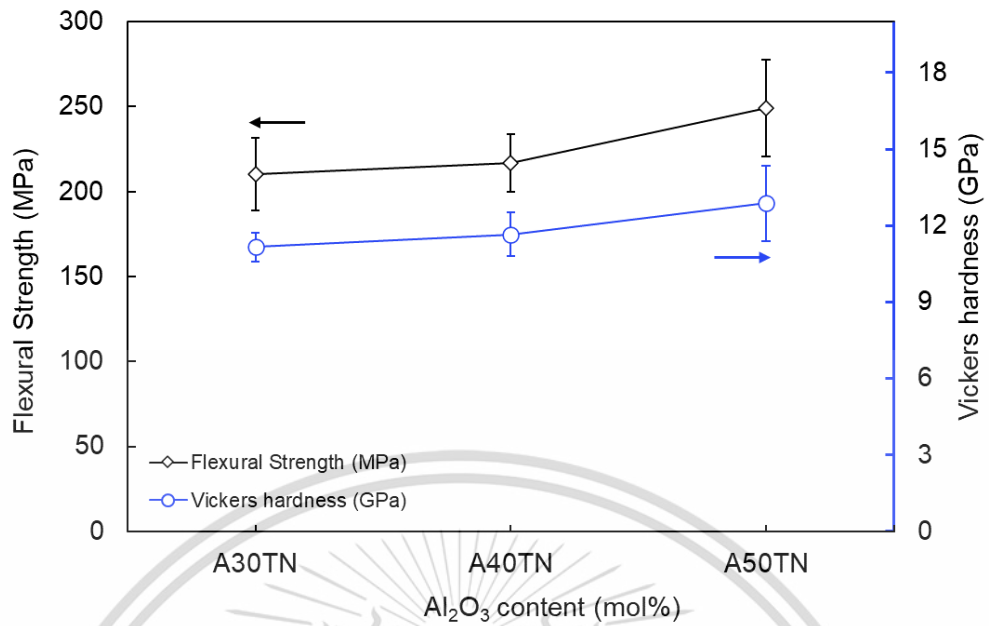


Figure 4.11 Flexural strength (black graph) and Vickers hardness (blue graph) of samples.

4.2.5 Corrosion behavior in molten Al

The corrosion behavior of composites was evaluated on the cross-section surface. Scanning electron microscopy-energy with dispersive X-ray spectroscopy (SEM-EDX) was employed to analyze the microstructure and chemical composition. An illustration of A30TN sample subjected to a 4 h corrosion test is demonstrated in Figure 4.11. From the image, it is discernible that aluminum underwent corrosion, penetrating into the surface of the A30TN sample to a thickness of approximately 54 μm . This observation signifies the extent of the corrosive interaction between the material and the molten aluminum.

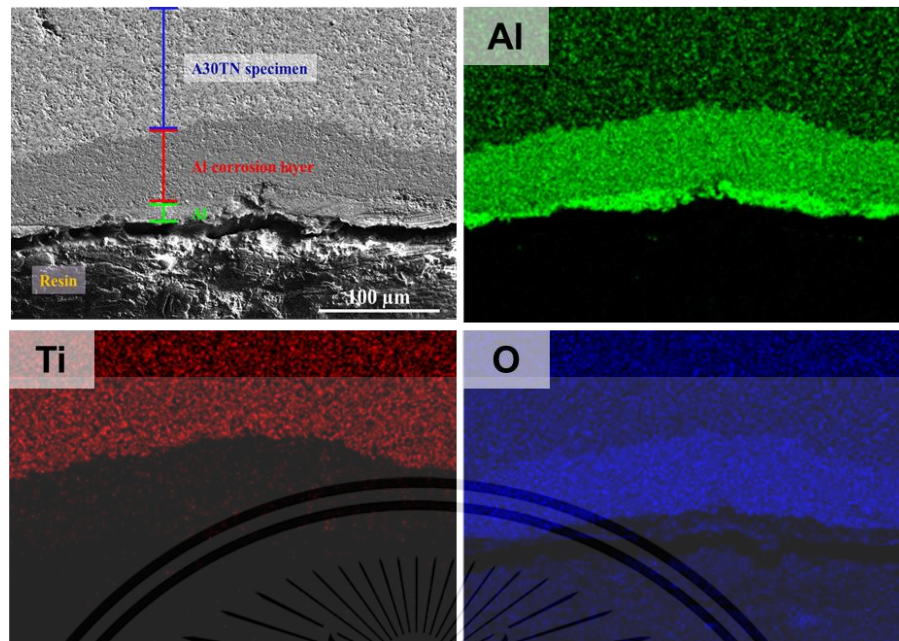


Figure 4.12 SEM image from the cross-section of the A30TN composite sample after immersion in molten Al at 720 °C for 4 h.

The examination findings revealed that the A30TN samples experienced significant corrosion when immersed in molten aluminum for 24 h and 48 h. Figures 4.12 and 4.13 present the corrosion layers for these respective time periods. Upon careful examination of the images, it appears that the surface of the A30TN samples exhibited substantial corrosion due to their interaction with the aluminum. Moreover, the degree of corrosion notably increased with prolonged immersion time. Specifically, the affected areas on the sample surfaces measured approximately 208 μm and 320 μm in thickness for 24 h and 48 h, respectively.

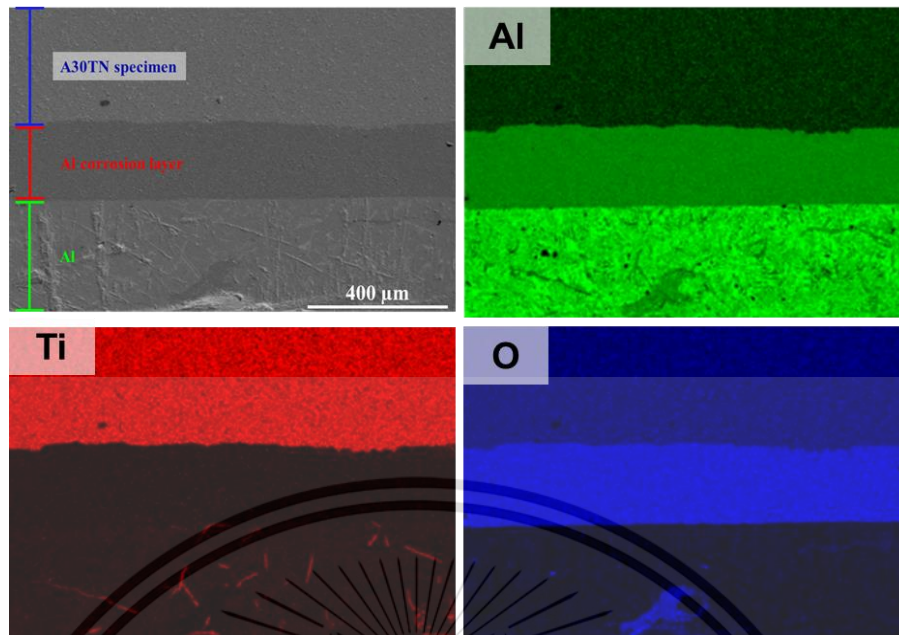


Figure 4.13 SEM image from the cross-section of the A30TN composite sample after immersion in molten Al at 720 °C for 24 h.

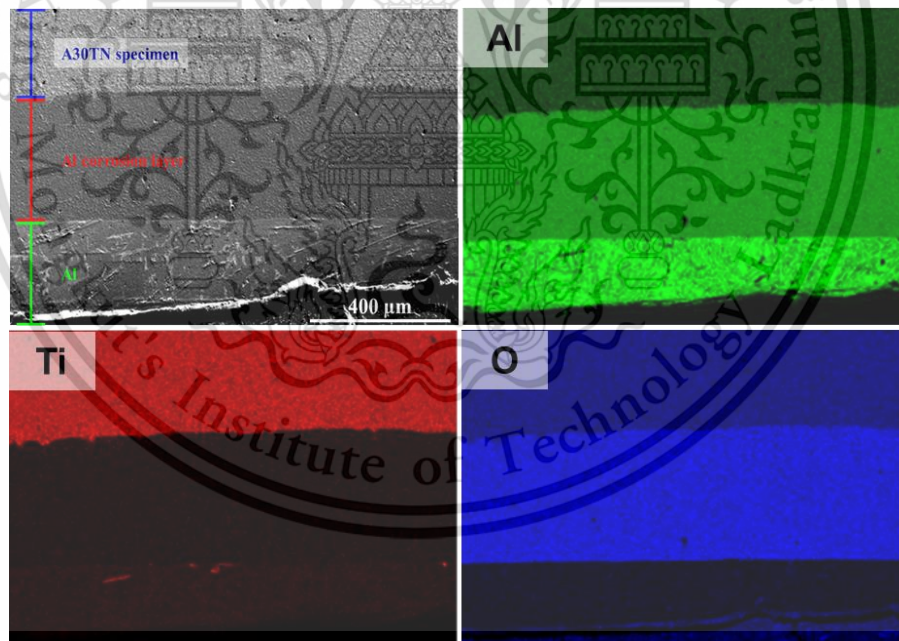


Figure 4.14 SEM image from the cross-section of the A30TN composite sample after immersion in molten Al at 720 °C for 48 h.

The results obtained from the corrosion testing of the A40TN sample, when exposed to liquid aluminum at 720°C for durations of 4, 24, and 48 h, are depicted in Figures 4.14, 4.15, and 4.16, respectively. An examination of these figures reveals a consistent pattern in the corrosion behavior exhibited on the surface of the A40TN samples. Specifically, there is a notable increase in corrosion intensity with prolonged immersion time. However, a distinctive observation is the comparatively lesser thickness of the corrosion layer, in contrast to what was observed in the A30TN sample. The thickness of the aluminum corrosion layer for the A40TN sample after immersion times of 4, 24, and 48 h are 53 μm , 177 μm , and 287 μm , respectively.

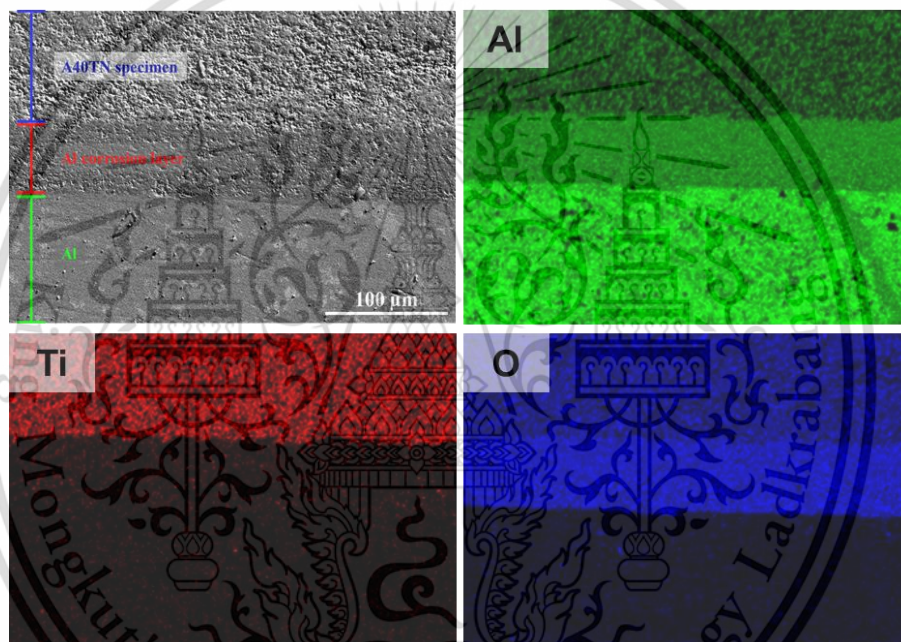


Figure 4.15 SEM image from the cross-section of the A40TN composite sample after immersion in molten Al at 720 °C for 4 h.

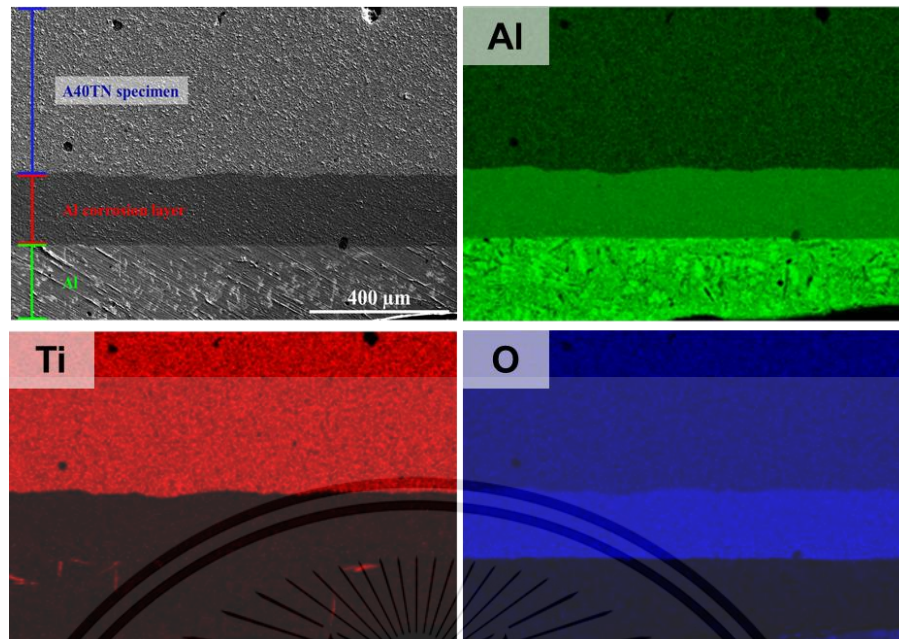


Figure 4.16 SEM image from the cross-section of the A40TN composite sample after immersion in molten Al at 720 °C for 24 h.

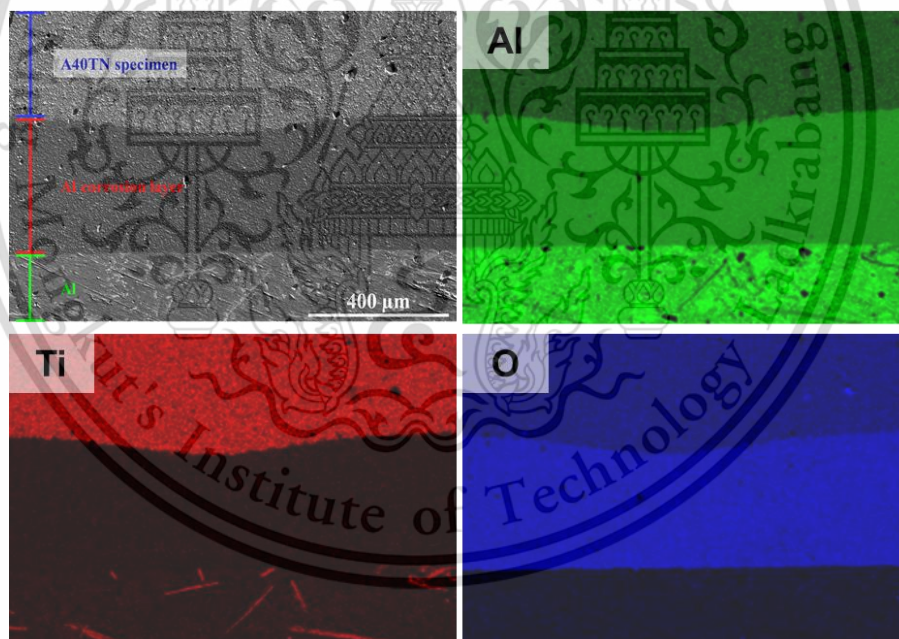


Figure 4.17 SEM image from the cross-section of the A40TN composite sample after immersion in molten Al at 720 °C for 48 h.

Figures 4.17, 4.18, and 4.19 illustrate the outcomes of the corrosion tests conducted on the A50TN sample. It is noteworthy that in the case of A50TN, no corrosion was evident at the 4 h immersion. However, the corrosion thickness increased to 120 μm and 247 μm at 24 and 48 h. These results align with the observed trend in

samples A30TN and A40TN. Notably, these images emphasize a clear escalation in corrosion with extended soaking times. However, what distinguishes the A50TN sample is the relatively lower degree of corrosion displayed, especially when compared to the preceding A30TN and A40TN samples. This could potentially be attributed to the higher density of such specimens, which also displayed the lowest porosity among all samples.

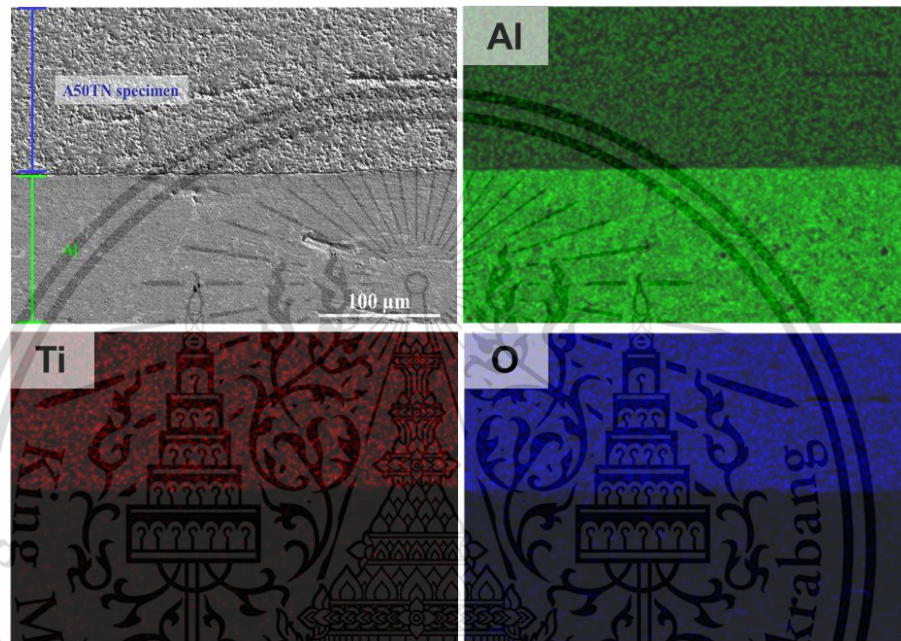


Figure 4.18 SEM image from the cross-section of the A50TN composite sample after immersion in molten Al at 720 °C for 4 h.

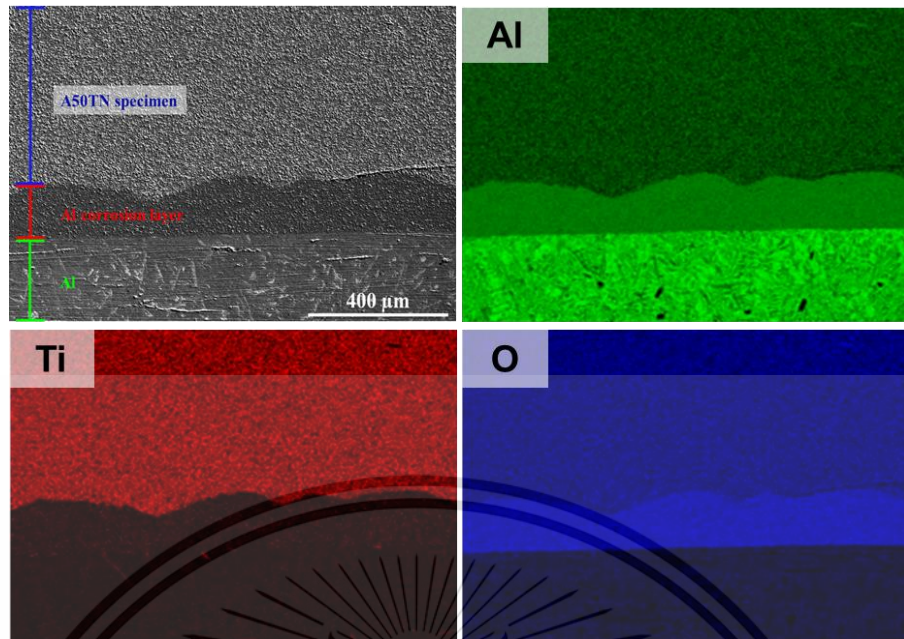


Figure 4.19 SEM image from the cross-section of the A50TN composite sample after immersion in molten Al at 720 °C for 24 h.

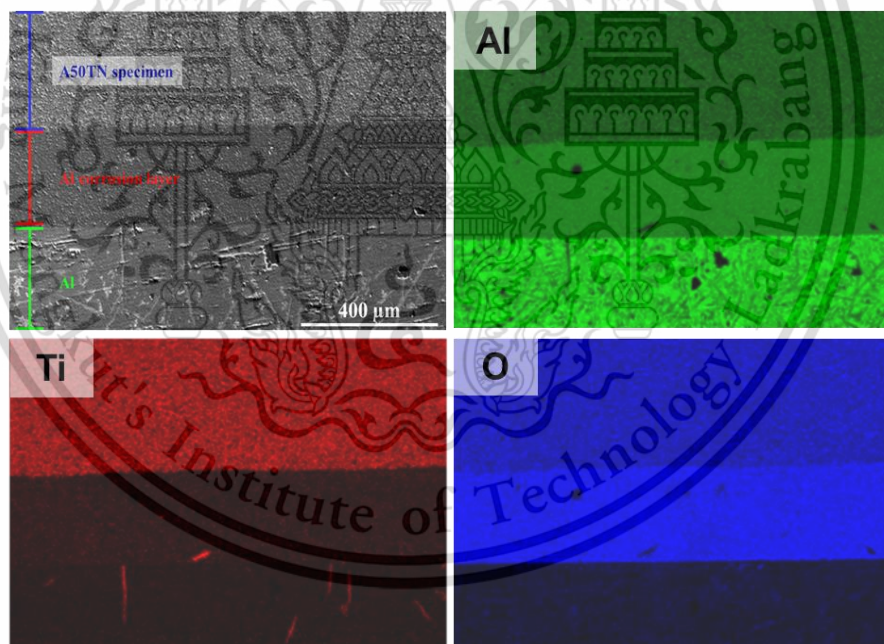


Figure 4.20 SEM image from the cross-section of the A50TN composite sample after immersion in molten Al at 720 °C for 48 h.

Figure 4.20 displays a comprehensive comparative analysis conducted by capturing images of each sample at different soaking durations. These visual representations effectively accentuated a consistent pattern observed across all samples, indicating a direct relationship between prolonged immersion time and the This material is reserved for educational use only, not allowed for commercial use.

Forbidden to modify the content, and cite the document when use.

corresponding increase in corrosion. This collective observation underscores the significance of exposure duration as a crucial factor influencing the extent of corrosion encountered by each sample.

Figure 4.21 depicts the thickness of the corroded layers for each sample, providing a detail of the corrosion behavior of A30TN, A40TN, and A50TN. The analysis revealed distinct corrosion layer thicknesses for each sample. Specifically, the A30TN sample showed a corrosion layer thickness of 54.48 μm , 208.16 μm , and 320.50 μm over the 4, 24, and 48 h, respectively. The A40TN sample demonstrated a narrower range of layer thickness compared to A30TN, with values of 53.20 μm , 177.46 μm , and 287.76 μm for the corresponding time intervals. Interestingly, the A50TN sample displayed the thinnest layer thickness, registering values of 0 μm , 120.87 μm , and 247.76 μm over the 4, 24, and 48 h periods. This observation underscores its superior resistance to corrosion compared to the other samples.

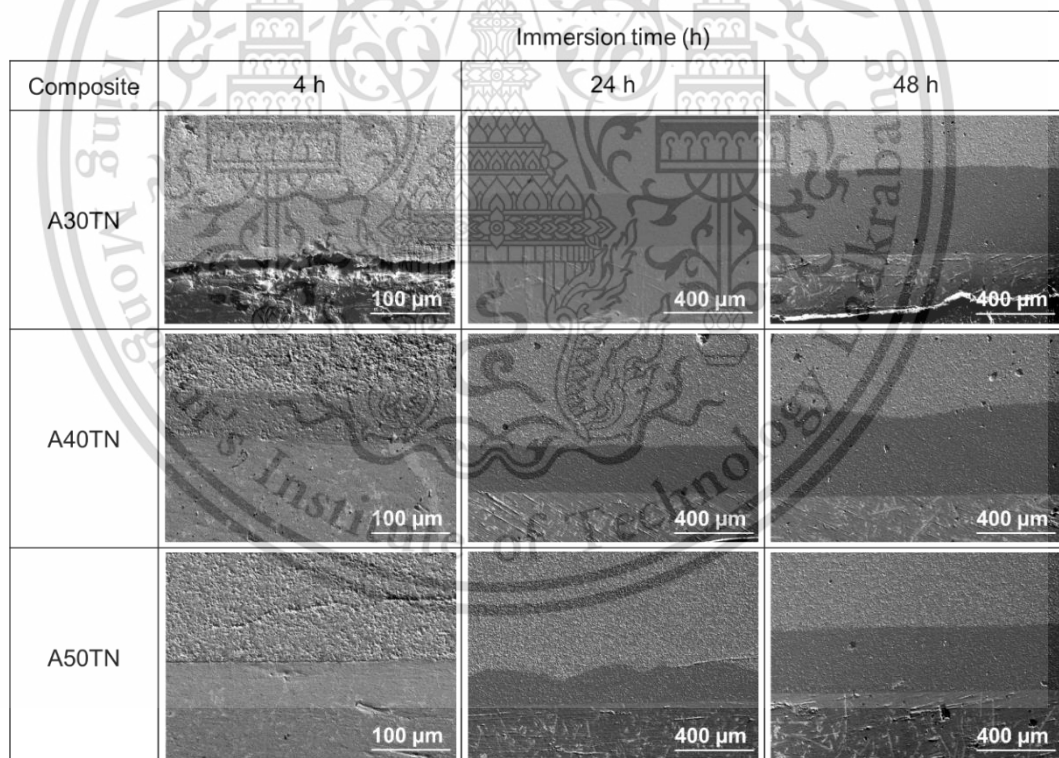


Figure 4.21 Comparison of the corrosion behavior of molten Al in all composites sample at 720 °C for 4, 24 and 48 h.

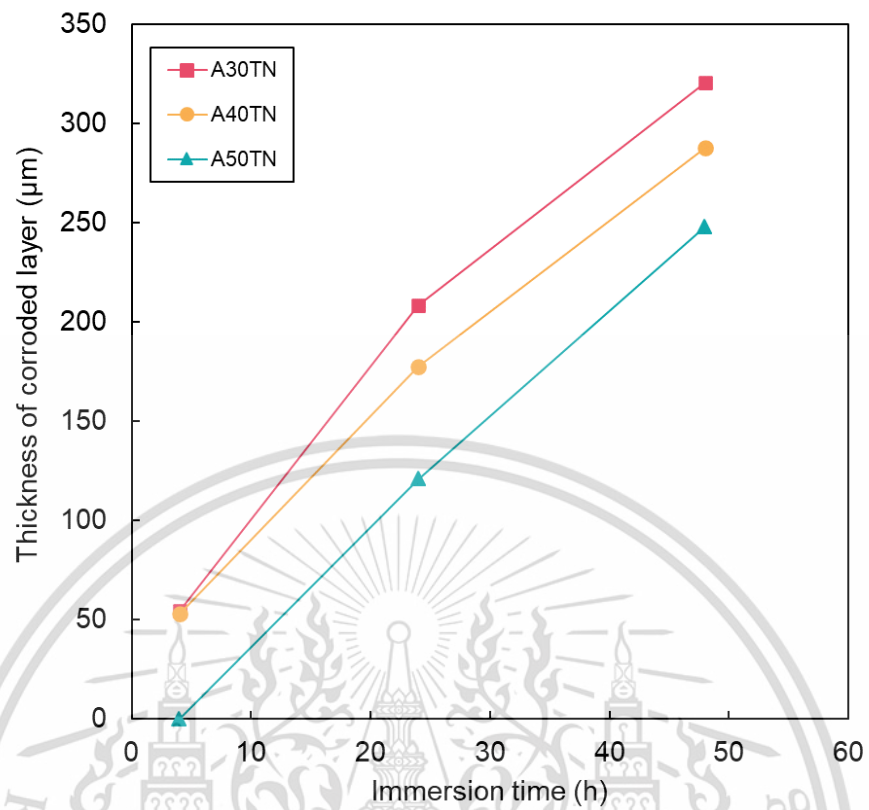


Figure 4.22 Plot of thickness of corroded layer in each range of all composite sample at 720°C.

Chapter 5

Conclusion

This thesis investigates the effects of additives, hexagonal boron nitride (h-BN) and aluminum nitride (AlN), on the properties of AT composites. The comprehensive study of phase transition, physical properties, mechanical properties, microstructure, and corrosion behavior in molten aluminum, demonstrating the relationship of these additives with the composite.

For h-BN addition, X-ray diffraction (XRD) analysis reveals the formation of aluminum borate ($\text{Al}_{18}\text{B}_4\text{O}_{33}$) in the ATBN composites. The content-dependent effect is observed, demonstrating a gradual increase in bulk density, reaching the highest value of 3.12 g/cm^3 in ATBN20, and a corresponding decrease in porosity to 2.75%. In addition, ATBN20 has a significant increase in mechanical properties, with flexural strength reaching 123.62 MPa and Vickers hardness reaching 11.15 GPa. Microstructural analysis confirms a reduction in pores with h-BN addition, which supports these findings.

For AlN addition, XRD results indicated the formation of Al_2O_3 and AT phases, with AlN contributing to the emergence of TiN. Increasing Al_2O_3 precursor content led to higher bulk density and lower porosity, with a maximum of 3.91 g/cm^3 in A50TN, accompanied by minimal porosity at 0.73%. Mechanical properties improve noticeably, with A50TN having the highest flexural strength (249.12 MPa) and Vickers hardness (12.87 GPa). SEM images illustrated a more extensive Al_2O_3 phase and TiN phase as the Al_2O_3 content increased. Mechanical testing revealed a direct correlation between Al_2O_3 content, flexural strength, and Vickers hardness. Corrosion behavior in molten aluminum highlighted the protective nature of the A50TN composite.

In summary, the incorporation of h-BN and AlN additives in AT composites influenced phase distribution, physical properties, microstructure, and mechanical properties. The reaction sintering process, aided by the additives, led to enhanced densification, resulting in improved mechanical performance. The findings provide valuable insights for the development of advanced ceramic composites for applications in refractory materials and structural components subjected to challenging conditions.

This material is reserved for educational use only, not allowed for commercial use.

Forbidden to modify the content, and cite the document when use.

References

- [1] Somiya, S., “Handbook of Advanced Ceramics: Materials, Applications, Processing, and Properties: Second Edition,” in **Handbook of Advanced Ceramics: Materials, Applications, Processing, and Properties: Second Edition**, Pp. 1–1229, 2013, doi:10.1016/C2010-0-66261-4
- [2] Hammel EC, Ighodaro OLR, and Okoli OI., “Processing and properties of advanced porous ceramics: An application-based review,” in **Ceramics International**, Vol. 40, no. 10, Pp. 15351-15370, 2014, doi:10.1016/j.ceramint.2014.06.095
- [3] Launey M. E. and Ritchie R. O., “On the fracture toughness of advanced materials,” in **Advanced Materials**, vol. 21, no. 20, Pp. 2103-2110, 2009, doi:10.1002/adma.200803322.
- [4] Hamano K., Ohya Y., and Nakagawa Z. e., “Crack propagation resistance of aluminum titanate ceramics,” in **International Journal of High Technology Ceramics**, Vol. 1, Pp. 129-137, 1985, doi:10.1016/0267-3762(85)90004-9
- [5] Maitra S., Bhattacharya S., Sil G., and Mondal S., “Aluminium Titanate Ceramics—A Review,” in **Transactions of the Indian Ceramic Society**, vol. 61, no. 2, 2002, doi: 10.1080/0371750X.2002.10800029
- [6] Hongzhi C., Guogang X., Chuanliang G., Lin J., and Wenlong Z., “Synthesis of porous Al_2TiO_5 ceramic by reaction sintering method,” in **Journal of the Ceramic Society of Japan**, vol.120, no. 1406, Pp. 413-416, 2012, doi:10.2109/jcersj2.120.413
- [7] Ewais, E. M. M., Besisa, N. H. A., and Ahmed, A., “Aluminum titanate-based ceramics from aluminum sludge waste,” in **Ceramics International**, vol. 43, no. 13, Pp.10277-10287, 2017, doi:10.1016/j.ceramint.2017.05.057
- [8] Ogunwumi, S. B., Tepesch, P. D., Chapman, T., Warren, C. J., Melscoet-Chauvel, I. M., and Tennent, D. L., “Aluminum titanate compositions for diesel particulate filters,” in **SAE Technical Papers**, 2005, doi:10.4271/2005-01-0583.
- [9] Babelot, C., Guignard, A., Huger, M., Gault, C., Chotard, T., Ota, T., and Adachi, N, “Preparation and thermomechanical characterization of aluminum titanate flexible ceramics,” in **Journal of Materials Science**, vol. 46, Pp.1211-1219, 2011, doi:10.1007/s10853-010-4897-2

- [10] Chen, W., Shui, A., Wang, C., Li, J., Ma, J., Tian, W., Ota, T., and Xi, X., "Preparation of aluminum titanate flexible ceramic by solid-phase sintering and its mechanical behavior," in **Journal of Alloys and Compounds**, vol. 777, 2019, doi:10.1016/j.jallcom.2018.09.317
- [11] H Thomas, H. A. J., Stevens, R., and Gilbert, E., "Effect of zirconia additions on the reaction sintering of aluminium titanate," in **Journal of Materials Science**, vol. 26, no. 13, Pp. 3613-3616, 1991, doi:10.1007/BF00557152.
- [12] Jiang, L., Chen, X. Y., Han, G. M., and Meng, Y., "Effect of additives on properties of aluminium titanate ceramics," in **Transactions of Nonferrous Metals Society of China (English Edition)**, vol. 21, no. 7, Pp. 1574–1579, 2011, doi:10.1016/S1003-6326(11)60899-6.
- [13] Chen, W., Shui, A., Shan, Q., Lian, J., Wang, C., and Li, J., "The influence of different additives on microstructure and mechanical properties of aluminum titanate ceramics," in **Ceramics International**, vol. 47, no. 1, Pp. 1169–1176, 2021, doi:10.1016/j.ceramint.2020.08.234.
- [14] Oikonomou, P., Dedeloudis, C., Stournaras, C. J., and Ftikos, C., "Stabilized tialite-mullite composites with low thermal expansion and high strength for catalytic converters," in **J Eur Ceram Soc**, vol. 27, no. 12, Pp. 3475-3482, 2007, doi:10.1016/j.jeurceramsoc.2006.07.020.
- [15] Perera, F. H., Pajares, A., and Meléndez, J. J., "Strength of aluminium titanate/mullite composites containing thermal stabilizers," in **Journal of the European Ceramic Society**, vol. 31, no. 9, Pp. 1695–1701, 2011
- [16] Zhao, Y. N., Chang, G., Liu, G., Song, H. B., and Zhang, W. L., "Preparation of mullite-aluminum titanate-cordierite multiphase ceramics," in **Advanced Materials Research**, Vol. 750–752, Pp. 484-487, 2013
- [17] Wang, Y., Wang, X., Liu, C., Su, X., Yu, C., Su, Y., Qiao, L., and Bai, Y., "Aluminum titanate based composite porous ceramics with both high porosity and mechanical strength prepared by a special two-step sintering method," in **Journal of Alloys and Compounds**, vol. 853, 2021, doi:10.1016/j.jallcom.2020.157193.
- [18] Shirai, T., Watanabe, H., Fujii, M., and Takahashi, M., "Structural Properties and Surface Characteristics on Aluminum Oxide Powders," in **Annual Report of the Advanced Ceramics Research Center Nagoya Institute of Technology**, vol. 9, 2009.

This material is reserved for educational use only, not allowed for commercial use.

Forbidden to modify the content, and cite the document when use.

- [19] Abyzov, A. M., "Aluminum Oxide and Alumina Ceramics (review). Part 1. Properties of Al_2O_3 and Commercial Production of Dispersed Al_2O_3 ," in **Refractories and Industrial Ceramics**, vol. 60, no. 1, 2019, doi:10.1007/s11148-019-00304-2.
- [20] Askeland, D.R., Phule, P.P., and Wright, W.J., "**The Science and Engineering of Materials: Sixth Edition**," in CT. Cengage Learning Stamford, Pp. 1-949, 2006
- [21] Allen, N. S., Mahdjoub, N., Vishnyakov, V., Kelly, P. J., and Kriek, R. J., "The effect of crystalline phase (anatase, brookite and rutile) and size on the photocatalytic activity of calcined polymorphic titanium dioxide (TiO_2)," in **Polymer Degradation and Stability**, vol. 150, 2018, doi:10.1016/j.polymdegradstab.2018.02.008
- [22] Wypych, A., Bobowska, I., Tracz, M., Opasinska, A., Kadlubowski, S., Krzywania-Kaliszewska, A., Grobelny, J., and Wojciechowski, P., "Dielectric properties and characterisation of titanium dioxide obtained by different chemistry methods," in **Journal of Nanomaterials**, vol. 2014, 2014, doi:10.1155/2014/124814.
- [23] Diebold, U., "The surface science of titanium dioxide," in **Surface Science Reports**, vol. 48, no. 5–8, 2003, doi:10.1016/s0167-5729(02)00100-0.
- [24] Benčina, M., Iglič, A., Mozetič, M., and Junkar, I., "Crystallized TiO_2 nanosurfaces in biomedical applications," in **Nanomaterials**, vol. 10, no. 6, 2020,
- [25] J Brant, J. A., Brunetta, C. D., and Aitken, J. A., "Chalcogenides and Nonoxides," in **Comprehensive Inorganic Chemistry II (Second Edition): From Elements to Applications**, vol. 5, 2013. doi:10.1016/B978-0-08-097774-4.00510-6.
- [26] Tsuji, Y., Kitamura, Y., Someya, M., Takano, T., Yaginuma, M., Nakanishi, K., and Yoshizawa, K., "Adhesion of epoxy resin with hexagonal boron nitride and graphite," in **ACS Omega**, vol. 4, no. 3, 2019, doi:10.1021/acsomega.9b00129.
- [27] Cheng, Z., Koh, Y. R., Mamun, A., Shi, J., Bai, T., Huynh, K., ... and Graham, S. (2020) "Experimental observation of high intrinsic thermal conductivity of AlN," in **Physical Review Materials**, vol. 4, no. 4, 2020, doi:10.1103/PhysRevMaterials.4.044602
- [28] Bachelard, R., and Joubert, P., "Aluminium nitride by carbothermal nitridation," in **Materials Science and Engineering A**, vol. 109(C), Pp. 247–251, 1989,
- [29] Mroz, T.J. Jr., "Annual Materials Review: Aluminum Nitride," in **American Ceramic Society Bulletin**, vol. 71, no. 5, Pp. 782–786, 1992.

- [30] Skala, R. D., Li, D., and Low, I. M., “Diffraction, structure and phase stability studies on aluminium titanate,” in **Journal of the European Ceramic Society**, vol. 29, no. 1, Pp. 67–75, 2009, doi:10.1016/j.jeurceramsoc.2008.05.037.
- [31] Kim, I. J., and Gauckler, L. G., “Formation, decomposition and thermal stability of Al_2TiO_5 ceramics,” in **Journal of Ceramic Science and Technology**, vol. 3, no. 2, Pp. 49-60, 2012, doi:10.4416/JCST2011-00049
- [32] Hono, T., Inoue, N., Morimoto, M., and Suzuki, Y., “Reactive sintering and microstructure of uniform, openly porous Al_2TiO_5 ,” in **Journal of Asian Ceramic Societies**, vol. 1, no. 2, Pp. 178–183, 2013, doi:10.1016/j.jascer.2013.05.004
- [33] Maki, R., and Suzuki, Y., “Microstructure and mechanical properties of MgO-doped Al_2TiO_5 prepared by reactive sintering,” in **Journal of the Ceramic Society of Japan**, vol. 121, no. 1415, Pp. 568–571, 2013, doi:10.2109/jcersj.2.121.568.
- [34] Park, S. Y., Jung, S. W., and Chung, Y. B., “The effect of starting powder on the microstructure development of alumina-aluminum titanate composites,” in **Ceramics International**, vol. 29, no. 6, Pp. 707–712, 2003, doi:10.1016/S0272-8842(02)00221-3.
- [35] Bueno, S., Moreno, R., and Baudín, C., “Reaction sintered $\text{Al}_2\text{O}_3/\text{Al}_2\text{TiO}_5$ microcrack-free composites obtained by colloidal filtration,” in **Journal of the European Ceramic Society**, vol. 24, no. 9, Pp. 2785–2791, 2004, doi:10.1016/j.jeurceramsoc.2003.08.015(2004).
- [36] Meybodi, S. M., Barzegar Bafrooei, H., Ebadzadeh, T., and Tazike, M., “Microstructure and mechanical properties of Al_2O_3 -20 wt% Al_2TiO_5 composite prepared from alumina and titania nano powders,” in **Ceramics International**, vol. 39, no. 2, Pp. 977-982, 2013, doi:10.1016/j.ceramint.2012.07.015.
- [37] Hernández M F, Suárez G, Cipollone M, Conconi M S, Aglietti E F, and Rendtorff N M 2017 Formation, microstructure and properties of aluminum borate ceramics obtained from alumina and boric acid **Ceram. Int.** 43 2188–2195
- [38] T. Sperisen, A. Mocellin, Investigation of the displacement reaction in mixed $\text{AlN}+\text{TiO}_2$ powders - Part I Microstructural changes at 1 atm N_2 , **J. Mater. Sci.** 27 (1992) 1121–1128.

- [39] Tanaka, M., Kashiwagi, K., Kawashima, N., Kitaoka, S., Sakurada, O., & Ohya, Y. (2012). Effect of grain boundary cracks on the corrosion behaviour of aluminium titanate ceramics in a molten aluminium alloy. **Corrosion Science**, 54(1), 90–96. <https://doi.org/10.1016/j.corsci.2011.09.002>
- [40] Kitiwan, M., Atong, D., Endo, F., & Goto, T. (2023). Effect of AlN addition on the reaction sintering of Al₂TiO₅ composites fabricated by spark plasma sintering. **J. Asian Ceram. Soc.**, 11(2), 225–231. <https://doi.org/10.1080/21870764.2023.2186008>



Author biography

Name	Paramapat Treetornkeerati (Aun)
Date of Birth	26 January 1995
Address	263 Moo. 2, Klondo Subdistrict, Dan Makham Tia District, Kanchanaburi, 71260
Education	(2007) Primary Education : Anubankanchanaburi School (2013) Middle-high school : Kanchananukroh School (2017) Bachelor's degree in Applied physics : King Mongkut's Institute of Technology Ladkrabang (2023) Master's degree in Applied physics : King Mongkut's Institute of Technology Ladkrabang
Work Experience	(2020) Position : NPI Supervisor Job description : Take care of new product projects to come out according to the needs of customers. Company : Draco PCB Co.,Ltd